MAPPING HYDROTHERMALLY ALTERED ROCKS AND LINEAMENT ANALYSIS THROUGH DIGITAL ENHANCEMENT OF ASTER DATA CASE STUDY: KEMASHI AREA, WESTERN ETHIOPIA

ABERA FANTAYE WELDEMARIAM

JULY, 2009

A thesis submitted to the School of Graduate Studies of Addis Ababa University in partial fulfillment of the requirements for the Degree Master of Science in Remote Sensing and GIS

ADDIS ABABA UNIVERSITY

SCHOOL OF GRADUATE STUDIES

MAPPING HYDROTHERMALLY ALTERED ROCKS AND LINEAMENT ANALYSIS THROUGH DIGITAL ENHANCEMENT OF ASTER DATA CASE STUDY: KEMASHI AREA, WESTERN ETHIOPIA

ABERA FANTAYE WELDEMARIAM

JULY 2009

GIS and Remote Sensing Program
Department of Earth Sciences

APPROVED BY EXAMINING BOARD:	SIGNATURE
Dr. Balemwal Atnafu Chairman, Department of Earth Sciences	_____
Dr. Dagnachew Legesse Adviser	_____
Dr. Gezahegn Yirgu Examiner	_____
Dr. Tesfaye Kidane Examiner	_____

To: My Mother

ACKNOWLEDGMENTS

I express my deepest gratitude and respect to my Adviser Dr. Dagnachew Legesse for his esteemed and constructive guidance and devoting his valuable time throughout the study.

My examiners, Dr. Gezahegn Yirgu and Dr. Tesfaye Kidane have gone through the manuscript and have given very important comments and corrections which greatly helped in improving the quality of this thesis and deservers many thanks.

Golden Prospect Mining Company PLC.(GPMC), merit great thanks for financial support and I extend my sincerely thanks to Dr. Kebede Hailu, General Manager of GPMC, Ethiopia, for his initiation and providing all support to carry out my study. Great thanks to all GPMC staffs.

I would like to thank Dr. Bedru Hussen for his valuable comments, discussion and support through out my study time and for his kind reviewing the manuscript and editorial efforts.

Special thanks go to Alazar Yosef, Alemayehu Mulachew, Bisrat Yebas, Girma Weldetinsae, Sheferawu Ayele, Sisay Lebasse and Yohans Belete, for providing me software, satellite images and literatures for my study.

My colleagues, Eyoel Muluwork, Tadesse Worku and Wodafrash Mamo have helped me in number of ways and deserve many thanks.

I am grateful to all my extended family and great thanks go to my brother Tezera, for his moral and material support.

I thank my wife, Tibebe and my daughters, Eden and Lucy. Your love, tolerance and support have contributed toward successful completion of my study.

TABLE OF CONTENTS

LIST OF TABLES

LIST OF FIGURES

ABSTRACT

Hydrothermal alteration, structure and geology of the Kemashi area, western Ethiopia have been studied by means of remote sensing techniques and limited field data. Advanced Spaceborn Thermal Emission and Reflection Radiometer (ASTER) reflectance data have been processed and interpreted with the production of geological map, lineament map and some hydrothermal alteration minerals abundance maps at a scale of 1:125,000.

Statistically selected and enhanced 3-bands color composite image of raw ASTER data and images resulted from principal component transformation (PCA) produced substantial spectral contrast between different lithology and enable to interpret the lithological boundaries.

Spatial enhancement of ASTER data using convolution filters and digital elevation model (DEM) extracted from the Shuttle Radar Topographic Mission (SRTM) have been used for lineament manual extraction. Hill-shading techniques are applied to SRTM DEMs to enhance terrain perspective views and to extract morphologically defined structures. Foliations, folds, different set of fractures are major structural elements recognized from the image processing and hill-shading techniques.

For regional mapping of some hydrothermal alteration minerals "Feature oriented Principal Component Analysis (FPCA)" and band rationing and threshold image processing methods were applied. For both methods application subset of the ASTER bands were selected according to the position of characteristics spectral features of the alteration minerals in the VNIR and SWIR portion of the spectrum.

Hydrothermal alteration in the study area mainly consist argillic-altered rocks and iron oxide/hydroxide altered rocks and mapped across various lithologic units.

The overall result of this study demonstrates the usefulness of remote sensing method and ASTER multi-spectral data for alteration, structure and lithologic mapping.

Keywords: alteration; ASTER; band ratio; digital elevation model; Ethiopia; geology; hydrothermal; Kemashi; lineament; lithology; PCA; SRTM, remote sensing; spectral.

1 INTRODUCTION

1.1 The Study Area

The study area is located in Western Ethiopia with in Oromia and Benishangul-Gumuz Regional States, approximately 500 km west of Addis Ababa. Its geographic boundary bounded by longitudes 35° 43′ 22″ E and 36° 24′ 41″ E, and 09° 21′ 16″ N and 09° 59′ 36″ N latitude and covers about an area of 4000 km^2 (Fig. 1).

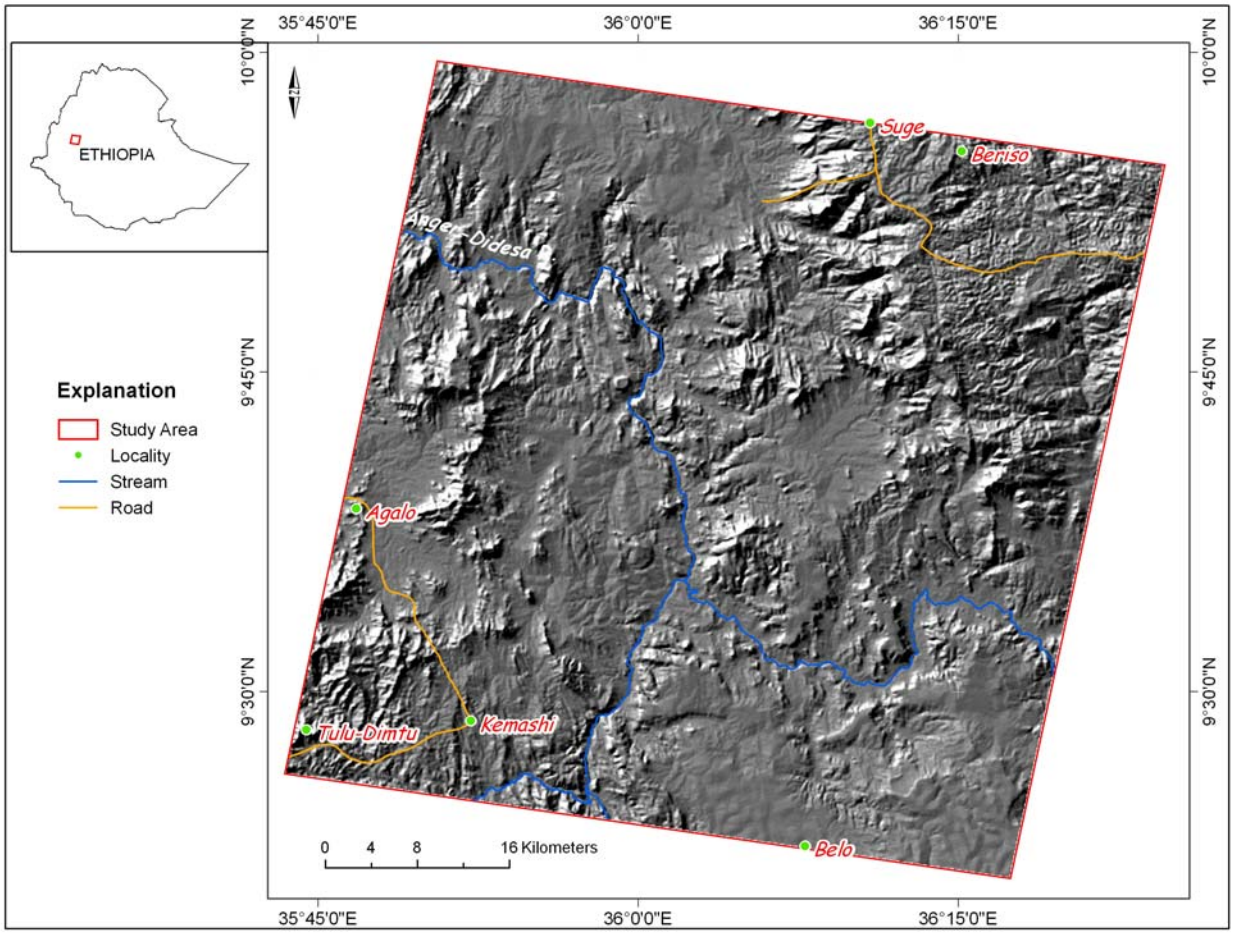

Figure 1. Geographic Location of the Study Area.

Road access to study area from Addis Ababa is via a sealed highway to Gimbi (440 km). The northeast and southwest quadrants are accessible by gravel-surfaced road. On the northwest and southeast of the area Anger river and its tributaries hinder the accessibility. Anger is the biggest river in the study area and flow northwest across the center of the study area.

The main rainy and dry seasons in the region are from June to August and between October and January, respectively and the mean annual rainfall is 1800 mm and the mean annual temperature is 20° C (Ethiopian Mapping Agency, 1981).

Elevation in the study area range from 600 to 2300m above sea level, and the area is mainly covered by the lowland physiographic landform with elevation range from 1000m to 1500m above sea level. The lowland area is covered by scattered thorn bushes and savanna grass cover; while the escarpment area is covered by sparsely growing trees (Solomon et al., 2000).

1.2 Previous Works

1.2.1 Regional Geology

The geology of Western Ethiopia was studied since late seventies, various workers with different objectives (eg. Kazmin, et al., 1979; deWite and Chewaka, 1981; Amenti, 1989). Western Ethiopia is covered by Precambrian basement rocks, Paleozoic-Mesozoic clastic and carbonate rocks and Cenozoic volcanic rocks.

In this region systematic geological mapping supported by Rb-Sr and U-Pb radiometric age dating was conducted by Ayalew et al., 1990. These Authors indicate that the Precambrian of western Ethiopia is constituted by high-grade gneisses, and low-grade metavolcano-sedimentary rocks which are the north and south continuation of Mozambique Belt (MB) and Arabo Nubian Shield (ANS), respectively. Pre-tectonic plutonic rock at 820 Ma and post-tectonic granites at 540 Ma intrude these rocks. Accordingly the tectonic history of the western Ethiopia basements is assumed to be consistent with about 1000-500 Ma, Pan-African evolution determined elsewhere in the Afro-Arabian Shield (e.g., Greenwood and other, 1976; Stern, 1994).

The sedimentary history began with the development of the contemporary rifts on the basement during the Late Paleozoic (Worton and Scarter, 1979). The North

easterly and north westerly trending trough was filled with continental sediments (Tamirat and Astin, 1992). Marin sediments resulted from the transgression of the sea covered most part of the Ethiopian land mass during Jurassic period (Getaneh, 1991).

The volcanic rocks classified as Trap series and Aden series represents the whole pile of the Tertiary flood basalt in the country (Mohr, 1962). These rocks cover the northwestern and southeastern plateau at the west margin of the main Ethiopian Rift Valley (Mohr, 1971; Mengesh et al., 1996).

1.2.2 Local Geology

The study area forms part on Gimbi and Nekemt map sheets. The geological map of both map sheets at scale of 1:250,000 were prepared and published by Geological Survey of Ethiopia (GSE). The Eastern 60% of the study area lies on Nekemt map sheet and 40 % lies on Gimbi map sheet. The geological map of the study area compiled from the previous works is shown on Fig. 2.

According to previous work the study area is covered by three major lithostratigraphic units. These are Precambrian crystalline basement rocks and associated intrusive, Paleozoic to Mesozoic Sedimentary rocks and Tertiary to Quaternary volcanic rocks (Solomon et al., 2000).

The Precambrian basement rocks and associated intrusives constitute the following lithologic units: 1) Metagranite 2) Metagabbro 3) Metaultramafics 4) Metavolcano-sedimentary schist 5) Quartz monzonite-monzodiorite 6) Quartzo-feldspathic gneiss 7) Biotite gneiss and 8) Undifferentiated gneiss.

The Protrozoic high grade metamorphic rocks consist of various gneisses and the low-grade metamorphic rock consists of metasedimentary–metavolcanic rocks. Large plutonic rocks of gabbroic and granite composition intrude the high-grade and low grade metamorphic rocks.

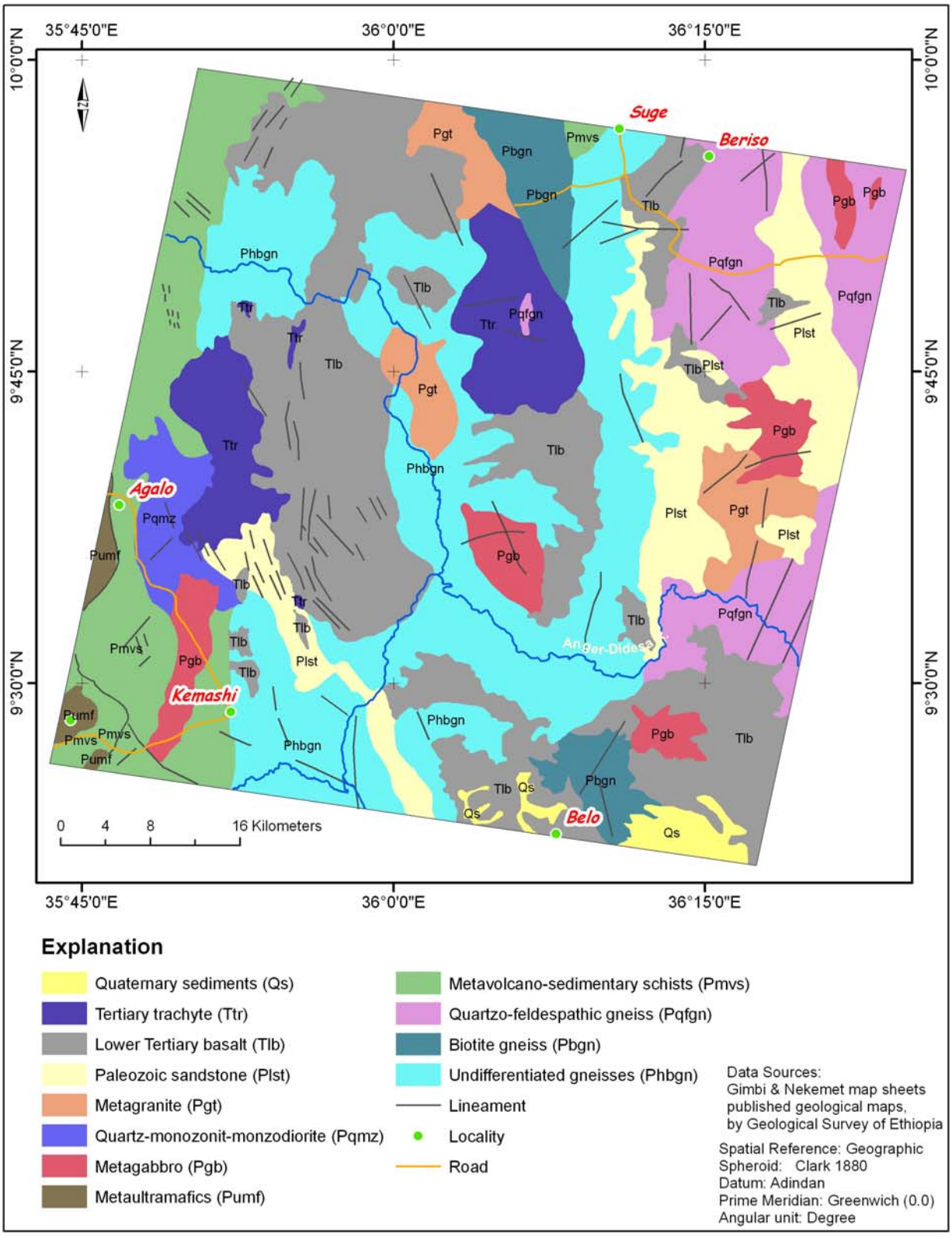

Figure 2. Geological map of the study area compiled from previous work.

According to Tadesse et al., 2000, the ultramafic and associated rocks mapped in Gimbi map sheet are affected by deformation and metamorphism and observed as linear tectonic belt marked the boundary of different litho-tectonic domains or as isolated small pods to continuous outcrops. According to Berhe, 1990, the ultramafic and associated rocks can be traced to north and south along strike as pan African Barka - Tulu Dimtu - Akobo-Sekerr ophiolitic suture. Only small part of the belt mapped in the southwest corner of the study area.

The Paleozoic–Mesozoic rocks represented by Paleozoic Sandstone and Interbeded siltstone, clay stone with subordinate shale. The Paleozoic sediments unconformable overlie the Precambrian basement rocks and underlie the Tertiary Volcanic rocks in the study area (Solomon et al., 2000).

The Tertiary volcanic rocks are classified into two main map units based on their mineralogical composition. These are: Tertiary lower basal and Tertiary Trachyte plugs and flows.

Different workers (Kazmin and other, 1979; Amenti, 1989; Ayalew and other, 1990) outlined polyphase deformation events for structural evolution of the crystalline basement rocks of western Ethiopia. Recent geological mapping of Gimbi and Nekemt map sheets support the idea of Ayalew et al., 1990, ocean closure and associated orogenic movement as bases for the structural evolution.

On the bases of deformation style, foliation trend and fold attitude, preserved in the Precambrian rocks, three phases of deformation events and designated as D1, D2 and D3 were recognized by earlier workers in the study area.

The first phase of deformation (D1) is the early deformation event and gave rise to a penetrative S1 foliation (Solomon et al., 2000). This deformation has a wide rang of trend from NNW to NNE and dips moderately to steeply dipping to west or east.

The second phase of deformation event (D2) is due to an east west progressive compression associated with plate convergence. It forms on early S1 surface (Solomon et al., 2000). The folds are close to tight and referred as F2 folds formed during D2 events.

The third phase of deformation (D3) has distinct NNE to NE trending en-echelon shear zone and extend for tens of kilometers along strikes with discontinuity due to Cenozoic cover (Solomon et al., 2000). The major structures with in the shear zones are: deformed foliation, lineation and folds. The D3-shear zones cross the D2 fabrics so are younger than D2 (Solomon et al., 2000).

The Precambrian and Phanarozoic rocks are traversed by two or more fracture systems. The fracture systems are very dense within the crystalline basement and form prominent features in the area.

2 OBJECTIVES OF THE STUDY

2.1 General Background

Lithologic and structural mapping is usually the first step in mineral exploration studies and commonly requires considerable field work. The use of multispectral remote sensing data and many ways of digital image enhancements techniques offer information so important in detecting the subtle features related to lithological variation and is therefore significant to facilitate and to confirm the field geological data acquisition and interpretation. Many studies have shown that maps produced from remotely sensed images can serve as adequate reconnaissance geological maps for mineral resource mapping (Rajesh, 2004). Further many studies have also shown that remotely sensed data could be employed to improve the existing maps of the area that was done by field method (e.g. Rothery, 1987; Abrams et al., 1988). Many studies also note that there is a strong correlation between mineral deposits and lineaments and emphasized the importance of lineament interpretation and analysis in localizing mineral deposits (e.g. Liu et al., 2000 and Rein and Kaufmann, 2003).

Mineral occurrences are commonly associated with hydrothermal alteration of the surrounding rocks, the style and extent of the alteration reflecting the type of mineral deposit. Alteration usually form zone around the mineralization which is larger than the deposit itself, therefore it provide information on area of mineralization. The delineation and characterization of hydrothermal alteration zone can therefore be of great value in mineral exploration and assessment of new prospecting sites. Several studies have shown the feasibility of remote sensing data to detect hydrothermally altered area (e.g. Hunt and Ashley, 1979 and Clark et al., 1990).

2.2 Specific objectives of the study

The present study intend to utilize remote sensing methods and techniques using Advanced Spaceborn Thermal Emission and Reflection Radiometer (ASTER)

multispecteral remote sensing data to extract geological information that may be use as initial bases for mineral exploration activities in the study area. The study also includes limited field work and use digital elevation data so as to make coherent geological information. In view of this the following were the specific objectives of the present study.

1. Improve existing geological map done by GSE using digital image processing techniques and visual image interpretation method.

2. Lineament mapping and analysis using digital image processing techniques and visual image interpretation method.

3. To identify and delineate hydrothermally altered zones using digital image processing techniques.

3 MATERIALS AND METHODS

3.1 Materials

Primary task of the present study encompasses gathering of relevant and available data that are essential to accomplish the study objectives, accordingly the following study material were used.

1. Single cloud-free Advanced Spaceborn Thermal Emission and Reflection Radiometer (ASTER) data recorded on February, 2002.

   This constitutes multispecteral bands and forms main data for the present geological studies.

2. The existing geological map covering the research study area.

   Parts of Gimbi and Nekemt map sheets geological maps. The map forms initial bases for identification of interpretation keys and knowledge on the type of litho-structural elements in the area.

3. Shuttle Radar Topography Mission (SRTM) digital elevation data, 90m x - y resolution.

   This data provides terrain relief and facilitate identification of geological structures.

4. Published Topographic maps of the area at 1:50,000 scale.

   This forms the geographic base map of the area and was essential for geo-referencing.

3.2 Methods

This study employees Remote Sensing and Geo-information system (GIS) methods and techniques and field visit. The objectives of the study were accomplished following an appropriate and systematically organized work process schematically shown in Fig. 3. Details of the methodological approaches with the theoretical backgrounds are presented in the following sections.

The image processing software ERDAS Imaging (Lica Geosystem) version 9.1 and ENVI (Environment for Visual Images) version 4.2 was used for remote sensing study. ArcGIS version 9.1 was utilized for the GIS data integration. StereoNet for Windows version 3.0 was used for lineament orientation analysis stereonet plot.

3.2.1 Data Preparation

3.2.1.1 Import ASTER EOS HDF data

The ASTER EOS HDF level-1B data was imported using ERDAS 9.1 (Lica Geosystems) image processing software with the firs-order polynomial transformation correction. The full subset of VNIR, SWIR and TIR bands were imported in geographic coordinate system. The imported images were path oriented. In order to transform the to north-up UTM, the images were re-projected using the following parameters: UTM Projection; Adindan Datum; UTM zone Number 37; Output image pixel size (X, Y): 15m (X), 15m (Y) and Nearest Neighbor re-sampling method.

The research area lies partly on Grid UTM zone 36 and partly on Grid UTM zone 37. To accommodate maps and images in both grid zones geographic coordinate system (spheroid: Clarke 1880) was used.

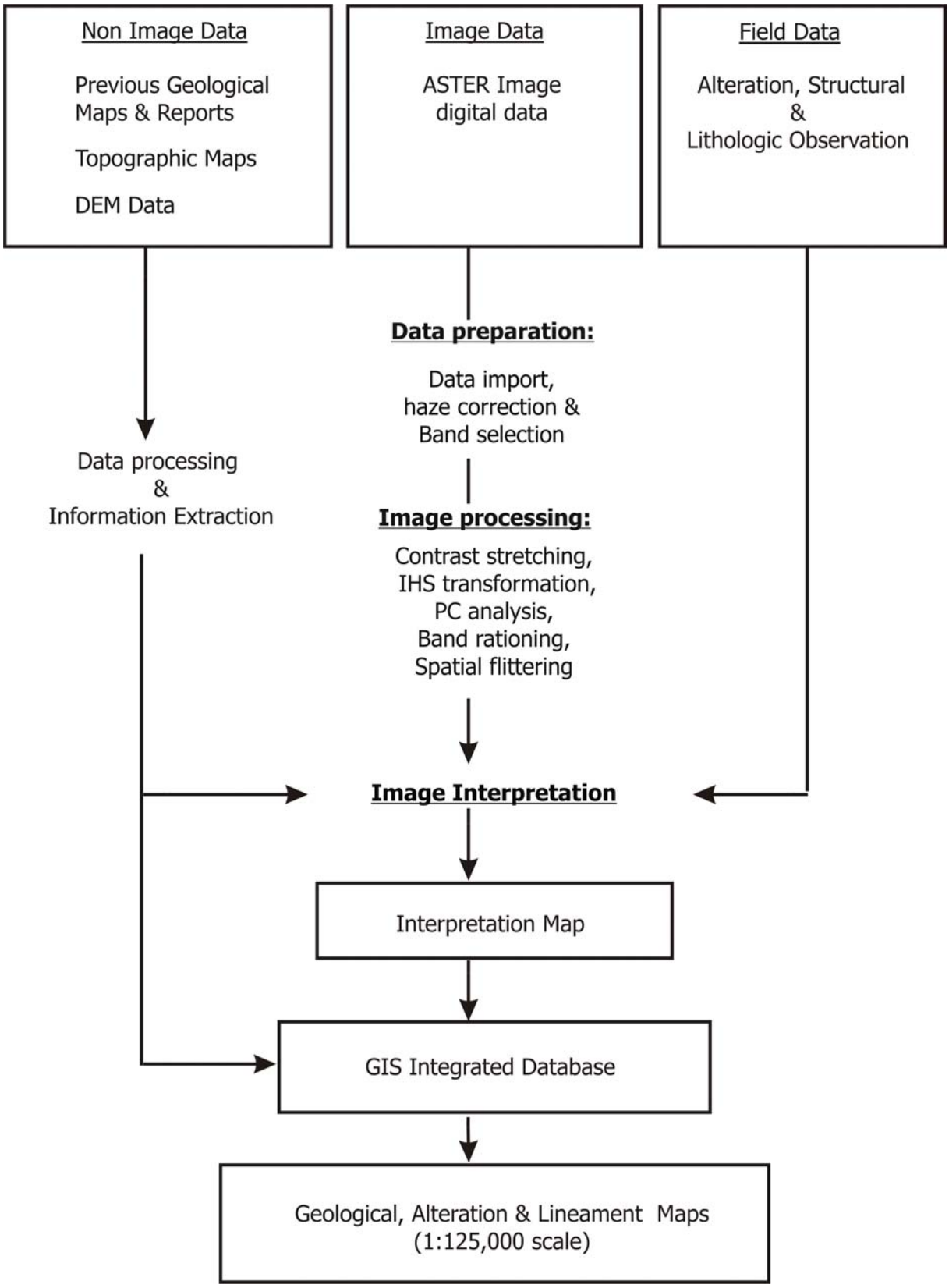

Figure 3. Schematic flow diagram showing the data and methodological procedures employed in this study

.

The ASTER spectral subset bands have deferent spatial resolutions. The visible and near infrared (VNIR) bands 1, 2 and band 3N are delivered at 15m resolution. The short wave inferred (SWIR) bands 4, 5, 6, 7, 8, and 9 are delivered at 30m resolution and the thermal inferred (TIR) bands 11, 12, 13 and 14 are provides in 90m resolution. The SWIR and TIR bands were re-sampled to 15m resolution to attain a consistent resolution for subsequent processing. The nearest neighbor algorithm was used during re-sampling so as to retain the original pixel grey values.

3.2.1.2 Band Selection

For the purpose of image display only three bands or band combinations, each directed to one of the primary color-gun (red, green, and blue), are required. In order to enhance a desired target and avoiding the redundancy of information spectral bands having the most information contents should be selected. Different workers demonstrate the possibility to select band combinations that contains the highest possible amount of information using statistical approach.

In this study, the optimum index factor (OIF) method introduced by Chavez et al., 1982 was adapted. The Optimum Index Factor (OIF) is a statistical calculation of every possible 3- band combination, based on total variance within bands and correlation coefficient between bands.

The index given by: OIF = $\sum_{i=1}^{3} SDi / \sum_{i=1}^{3} ABC(CCi)$

Where SDi is the standard deviation of band i and ABC (CCj) is the correlation coefficient between any two of the possible three pairs. The highest value of OIF should be the three bands having the most information content (Chavez et. al. 1982). This measure favors the selection of those bands having high variance and low pair-wise correlation. Table (1, 2 & 3) presents the statistical parameters necessary for the calculation of OIF for the 9 bands (VNIR & SWIR) of ASTER image of the study area.

Table 4, presents the OIF values for each possible 3-band combination. The minimum OIF value 5.915 represented by band combination 9, 7 and 6. This low value OIF indicates, a high degree of correlation between the bands resulting the lowest relative "data richness" for this particular image. The band combination 8, 3 and 1 have the maximum OIF value of 21.06 and that a low correlation between the three bands. The bands represent one band from each of the three spectral classes (Shortwave Inferred, Near Inferred, and Visible), which would be expected to exhibit different reflective qualities.

Various band combinations were visually inspected to support the statistical method, and most of the high rank band combinations give helpful geological information. The band combination 8, 4 and 2 with the lowest OIF at rank number 50 provide good color contrast between different lithologic units and structures also apparently enhanced.

3.2.1.3 Haze Correction

Space born optical sensors recording data in the visible and shortwave inferred spectrum receive solar radiation reflected from the Earth's surface and radiation scattered by the atmosphere. Since the atmospheric effect due to haze, aerosol, etc. modifies the radiation reflected at the ground reducing image contrast, and contributes an additive term, correction is necessary in order to convert the "at sensor" or "top-of-atmosphere" radiance to ground leaving radiance.

To determine the portion of the at-sensor or radiance that is attributable to ground properties, while subtracting out the portion that is attributable to atmospheric effects in the situation when actual atmospheric data are note available is done by "dark object subtraction" approach given by Crane, 1971. The method is based on the assumption that the atmospheric scattering throughout the scene is uniform and somewhere in the image there is a pixel with zero reflectance, such that the radiometric contribution from this pixel represent only the additive term.

Table 1. Statistical attributes of ASTER image raw data used in this study.

Bands	**1**	**2**	**3**	**4**	**5**	**6**	**7**	**8**	**9**
Minimum	45.00	27.00	19.00	7.00	1.00	1.00	1.00	1.00	1.00
Maximum	142.00	139.00	124.00	255.00	255.00	255.00	255.00	255.00	255.00
Mean	71.79	57.87	54.61	61.28	49.57	53.24	48.24	44.88	40.87
Median	71.00	57.00	54.00	62.00	50.00	53.00	48.00	45.00	41.00
Mode	70.00	57.00	53.00	65.00	51.00	55.00	49.00	45.00	40.00
SD	11.23	6.53	7.83	6.61	6.62	5.04	6.61	6.62	5.04

Table 2. Covariance matrix of ASTER image used in this study.

Band	**1**	**2**	**3**	**4**	**5**	**6**	**7**	**8**	**9**
1	57.11	73.62	29.83	55.71	35.48	43.20	33.75	31.75	22.24
2	73.62	102.14	45.66	83.28	51.30	62.60	48.88	46.21	33.44
3	29.83	45.66	132.93	93.83	33.24	38.11	24.21	18.18	19.66
4	55.71	83.28	93.83	126.99	64.67	77.29	58.31	52.09	40.91
5	35.48	51.30	33.24	64.67	42.56	50.21	41.20	39.74	29.80
6	43.20	62.60	38.11	77.29	50.21	61.32	49.83	48.19	35.86
7	33.75	48.88	24.21	58.31	41.20	49.83	43.26	42.19	31.08
8	31.75	46.21	18.18	52.09	39.74	48.19	42.19	43.34	31.56
9	22.24	33.44	19.66	40.91	29.80	35.86	31.08	31.56	25.23

Table 3. Correlation matrix for ASTER image used in this study,

Band	**1**	**2**	**3**	**4**	**5**	**6**	**7**	**8**	**9**
1	1.00								
2	0.96	1.00							
3	0.34	0.39	1.00						
4	0.65	0.73	0.72	1.00					
5	0.72	0.78	0.44	0.88	1.00				
6	0.73	0.79	0.42	0.88	0.98	1.00			
7	0.68	0.74	0.32	0.79	0.96	0.97	1.00		
8	0.64	0.69	0.24	0.70	0.92	0.93	0.97	1.00	
9	0.59	0.66	0.34	0.72	0.91	0.91	0.94	0.95	1.00

Table 4. OIF Values for all possible 3-band Combinations of ASTER VNIR & SWIR (9 bands) spectral subset.

Rank	3-band	SUM_SD	SUM_CC	OIF		Rank	3-band	SUM_SD	SUM_CC	OIF
1	1,3,8	25.66	1.22	21.06		**43**	1,4,6	22.88	2.26	10.12
2	1,3,7	25.65	1.34	19.15		**44**	1,6,8	22.89	2.30	9.94
3	1,3,9	24.08	1.27	19.02		**45**	1,2,5	24.15	2.46	9.81
4	1,3,6	26.88	1.49	18.00		**46**	3,4,6	19.48	2.02	9.65
5	1,3,4	30.28	1.72	17.63		**47**	1,6,7	22.88	2.38	9.63
6	1,2,3	29.12	1.70	17.17		**48**	1,6,9	21.31	2.23	9.57
7	1,3,5	25.57	1.50	17.02		**49**	1,5,6	22.89	2.43	9.41
8	2,3,8	20.99	1.32	15.85		**50**	2,4,8	19.76	2.13	9.29
9	2,3,7	20.97	1.44	14.51		**51**	2,4,7	19.74	2.25	8.76
10	2,3,9	19.40	1.39	13.97		**52**	2,4,9	18.17	2.11	8.60
11	3,7,8	21.06	1.53	13.75		**53**	2,4,5	19.76	2.39	8.27
12	3,5,8	21.08	1.61	13.13		**54**	2,5,8	19.77	2.40	8.25
13	2,3,5	20.99	1.61	13.03		**55**	2,7,8	19.76	2.40	8.22
14	3,8,9	19.49	1.53	12.72		**56**	4,7,8	19.84	2.46	8.05
15	3,4,8	21.06	1.66	12.67		**57**	2,5,7	19.76	2.47	7.99
16	1,2,4	28.85	2.35	12.28		**58**	4,5,8	19.85	2.51	7.92
17	1,4,8	24.46	1.99	12.27		**59**	2,8,9	18.19	2.31	7.88
18	3,5,7	21.06	1.72	12.25		**60**	2,7,9	18.17	2.33	7.78
19	3,6,8	19.49	1.59	12.22		**61**	2,5,9	18.19	2.35	7.75
20	3,7,9	19.48	1.60	12.19		**62**	4,8,9	18.27	2.38	7.68
21	2,3,6	19.40	1.60	12.10		**63**	2,4,6	18.17	2.40	7.58
22	1,4,9	22.88	1.96	11.66		**64**	4,5,7	19.84	2.63	7.55
23	3,5,9	19.49	1.69	11.54		**65**	2,6,8	18.19	2.42	7.52
24	1,4,7	24.45	2.12	11.53		**66**	4,7,9	18.25	2.45	7.45
25	3,4,7	21.05	1.83	11.52		**67**	2,6,7	18.17	2.49	7.29
26	3,6,7	19.48	1.71	11.41		**68**	4,5,9	18.27	2.51	7.27
27	2,3,4	20.97	1.84	11.37		**69**	4,6,8	18.27	2.51	7.27
28	3,4,9	19.48	1.78	10.92		**70**	2,5,6	18.19	2.55	7.13
29	1,4,5	24.46	2.25	10.86		**71**	2,6,9	16.60	2.36	7.03
30	1,5,8	24.48	2.28	10.72		**72**	5,7,8	19.85	2.86	6.94
31	3,6,9	17.91	1.67	10.71		**73**	4,6,7	18.25	2.63	6.94
32	1,7,8	24.46	2.29	10.68		**74**	4,5,6	18.27	2.74	6.67
33	3,5,6	19.49	1.85	10.56		**75**	4,6,9	16.68	2.51	6.65
34	1,2,8	24.24	2.30	10.55		**76**	5,8,9	18.28	2.79	6.56
35	1,8,9	22.89	2.18	10.51		**77**	5,7,9	18.27	2.81	6.50
36	1,7,9	22.88	2.21	10.37		**78**	5,6,8	18.28	2.84	6.43
37	1,5,7	24.46	2.36	10.37		**79**	7,8,9	18.27	2.87	6.37
38	1,5,9	22.89	2.21	10.34		**80**	6,7,8	18.27	2.88	6.35
39	3,4,5	21.06	2.04	10.31		**81**	5,6,7	18.27	2.91	6.28
40	1,2,9	22.66	2.21	10.26		**82**	6,8,9	16.69	2.80	5.96
41	1,2,6	25.45	2.48	10.24		**83**	5,6,9	16.69	2.80	5.95
42	1,2,7	24.23	2.38	10.19		**84**	6,7,9	16.68	2.82	5.92

Based on this approach to estimate the upwelling scattered path radiance due to atmospheric haze for each ASTER band, the histogram of data values examined and shifted toward lower grey value by constant that is supposed to represent the additive term of haze. Accordingly, for the study area ASTER scene the subtracted gray values are 45, 27, 19 and 7 for ASTER Band 1 through 4 and gray value 1, for ASTER Band 5 through 9, respectively in order to obtain a gain of zero.

3.3 Image Enhancement

ASTER data was digitally processed and several enhancement techniques namely: contrast stretching, HIS transformation, principal component analysis (PCA), band rationing and spatial filtering were applied. The enhancement gave substantial results in geological interpretation is briefly summarized in the following section.

3.3.1 Linear Contrast Enhancement

Contrast enhancement is one of the most widely used image processing techniques for geological studies. It is the process of redistributing the brightness levels in an image to utilize the entire dynamic range of the display device. In order to produce an enhanced image during data processing the raw data stretch over the quantized range of grey value (256 for 8-bit data). The resulting enhancement, however, is strongly controlled by mean and standard deviation statistics of the input data and consequently influences the resulting color in image composites since they regulate the brightness of the bands under consideration and thus the corresponding colors.
For this study the stretched images have been interpreted for lithologic and lineament interpretation.

3.3.2 IHS Transformation

IHS transformation is a process in which a bands RGB composite is decomposed into intensity (I), hue (H), and saturation (S) components and after manipulated then it is transformed back to the RGB-space for interpretation (Sabins, 1987).

Intensity represents the brightness, hue signifies the dominant wave length, and saturation is related to purity of a color (Sabins, 1987). The advantage of this technique is its ability to effectively separate intensity and spectral information from standard image, and the possibility to convert HIS elements back to RGB -space. The resulting enhanced color images are easier to interpret, as the spectral information (hue) is not changed during transformation.

3.3.3 Principal Component Analysis (PCA)

The "principal component analysis transformation", is a multivariate statistical method used to compress multi spectral dataset into few PC images in which spectral difference between materials become apparent in PC image than individual bands (Sabins, 1987; Gillespie et al., 1986). Principal components are commonly calculated using the covariance matrix obtained from the input multi-spectral data where by the corresponding eigenmatrices is also determined.

In this study, PCA was performed on ASTER data covering the 9 wavelength bands (VNIR and SWIR). For lithologic discrimination and the color composite created from the PC images gives valuable geological information.

Feature oriented principal component analysis (FPCA) was also applied to subsets of ASTER bands (VNIR & SWIR) for identification of key alteration mineral using the Crosta techniques proposed by Loughlin (1991).

3.3.4 Band Rationing

This procedure involves the division of two bands, where the band with high reflectance features of the given material is assigned as numerator, while the other band with high absorption feature for the same material is assigned as denominator. Rationing can be thought as a method of enhancing minor difference between materials by defining the slope of the spectral curve between two bands. The resultant gray-scale band ratio image is not a direct measurement for the material's contents, rather it mark the area with highest possibilities for the presence of the given material. The combination of three-band ratio image as red-green-blue (RGB) image is useful for the interpretation of the result.

Ratio images have been used in many geological investigations to recognize and map areas of mineral alteration (Rowan et al., 1974; Vincent, 1975) and for lthologic mapping (Gotez et al., 1975; Blodget et al., 1975).

In this study ratio image is mainly used for mineral alteration mapping. ASTER bands selected for band rationing for mineral alteration mapping is based on alteration minerals reflectance features.

3.3.5 Spatial Enhancements

One of the characteristic features of the satellite images is a parameter called spatial frequency which is defined as the number of changes in brightness value per unit distance for any particular part of an image. If there are very few changes in brightness value over a given area in an image, this is referred to as a low-frequency area. Conversely, if the brightness values change dramatically over short distance, this is an area of high frequency (Jensen, 1996). Spatial filters emphasize or deemphasize image data of variable frequencies that refer to the "roughness" of the total variation (Lillesand, et al., 2004). The process involves matrix operations where the spatial distribution of the pixel and the moving window size play an influential role. Filters that operate in the frequency domain are implemented through the

Fourier transformation, whereas those which operate in the spatial domain of the image itself are known as convolution filters (eg. List, 1993).

In this study spatial enhancement is manly applied to facilitate visual interpretation of ASTER image for the purpose of lineament mapping using convolution filters. For the smaller and medium size lineament identification the mid-low filters of 3x3 window edge detection filters known as *Gradient-Soble* and *Gradient-Prewitt* were utilized and for the larger lineaments 7x7 widow size directional filters were used, adapted from Kenea, 1997.

3.4 Image Interpretation

The visual interpretation of lithology, lineament and mineral alteration was performed by applying image interpretation keys, such as color (tone), texture, shapes, patterns and interrelationship between features that may have geological significance. Data from the existing geological maps and limited filed visit were utilized for image interpretation and verification of results obtained from digital image processing.

In order to understand geological significant of lineaments and easy of data interpretation the lineaments were grouped into domains, based on relative homogeneity of measured linear features.

3.5 Application of Geographic Information System (GIS)

A Geographic Information System (GIS) is a computer system for managing spatial data. GIS are designed to bring together spatial data from diverse sources in to a unified database, often employing different digital data structures and representing spatially varying phenomenon as serious of data layers.

For this study different data layers that individually represent part of the spatial information system relevant to the study area have been used. In this study GIS was primarily applied for the purpose of data integration, visualization, and cartographic work and for limited data analysis. All the digital data organized in the GIS database have been spatially registered using geographic coordinate with spheroid of Clarke 1880.

4 REMOTE SENSING AND GEOLOGY

4.1 Background

"Remote Sensing" is the science and art of obtaining information about an object, or phenomenon through the analysis of data acquired by a device that are not in contact with the object, area or phenomenon under investigation (Lillesand, Kiefer & Chipman, 2004).

In remote sensing, information transfer is accomplished by use of electromagnetic radiation (EMR). In respect to type of energy resources two types of remote sensing are known, namely, passive and active remote sensing. Passive remote sensing is sensor that detects the reflected or emitted electro-magnetic radiation from the natural sources. Active remote sensing detects reflected responses from objects that are irradiated from artificially generated energy sources.

Based on wavelength region, remote sensing classified into four main categories, these are Visible, Reflected Infrared, Thermal and Microwave remote sensing.

Several important innovations in remote sensing were made in the first half of the twenty century. The most important developments to the geologist were systematic images of the Earth's surface by the three Landsat satellites. During the last few years, the role of remote sensing has been examined and utilized widely as an aid in mineral exploration.

Anomalous limonitic rocks, which can be a potential indicator of hydrothermal alteration, can be mapped at 79m spatial resolution in the MSS band (Rowan et. al., 1974; Schmidt, 1976).

The Landsat Thematic Mapper (TM) extends the spectral range to the SWIR region by adding bands at 1.65 and 2.20 μm, and the spatial resolution was also improved to 30m. Selection of 2.2 μm band (TM band 7) was based on laboratory and field

spectral reflectance measurements. In this wavelength region clay, carbonate, sulfate, and hydrous minerals exhibit spectral absorption feature due to molecular vibrational process. (Fig. 4)

The spectral band (TM band 7) and the band located at 1.65 μm (TM band 5) greatly increased discriminating hydrothermally altered rocks, but because of the breadth of TM band 7 some hydrothermally altered rock that contain minerals such as alunite and kaolinite (2.17 and 2.2 μm absorption feature) are commonly difficult to distinguish spectrally in TM images, because both have absorption features located in TM band 7.

The spectral bands of the ASTER SWIR sub-system were designed to measure reflected solar radiation in one band at 1.6 μm, and five bands in the 2.10 – 2.45 μm region in order to distinguish Al-OH, Fe, Mg-OH, H-O-H and CO_3, absorption features (Fig. 5).

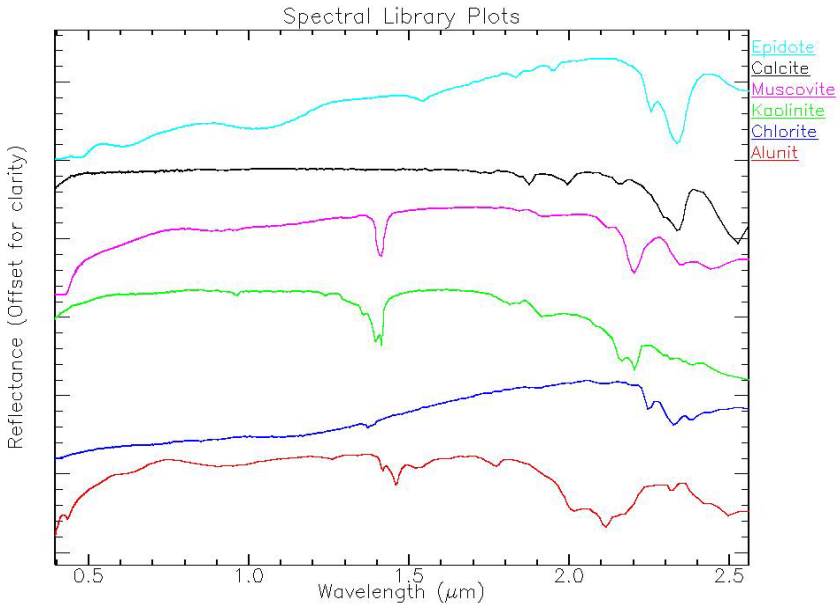

Figure 4. Laboratory spectra of epidote, calcite, muscovite, kaolinite, chlorite, and alunite Which are common hydrothermal alteration minerals (Clark et al., 1993b).
Alunite and kaolinite have Al-O-H absorption features at 2.17 and 2.20 μm. Muscovite has a prominent Al-O-H 2.20 μm absorption feature and a secondary 2.32 μm absorption feature. Chlorite and epidote have a Fe-Mg-O-H 2.35 μm absorption feature and a broad Fe^{2+} feature from 1.65 to 0.6 μm. Calcite has a prominent 2.33 μm CO_3 absorption feature.

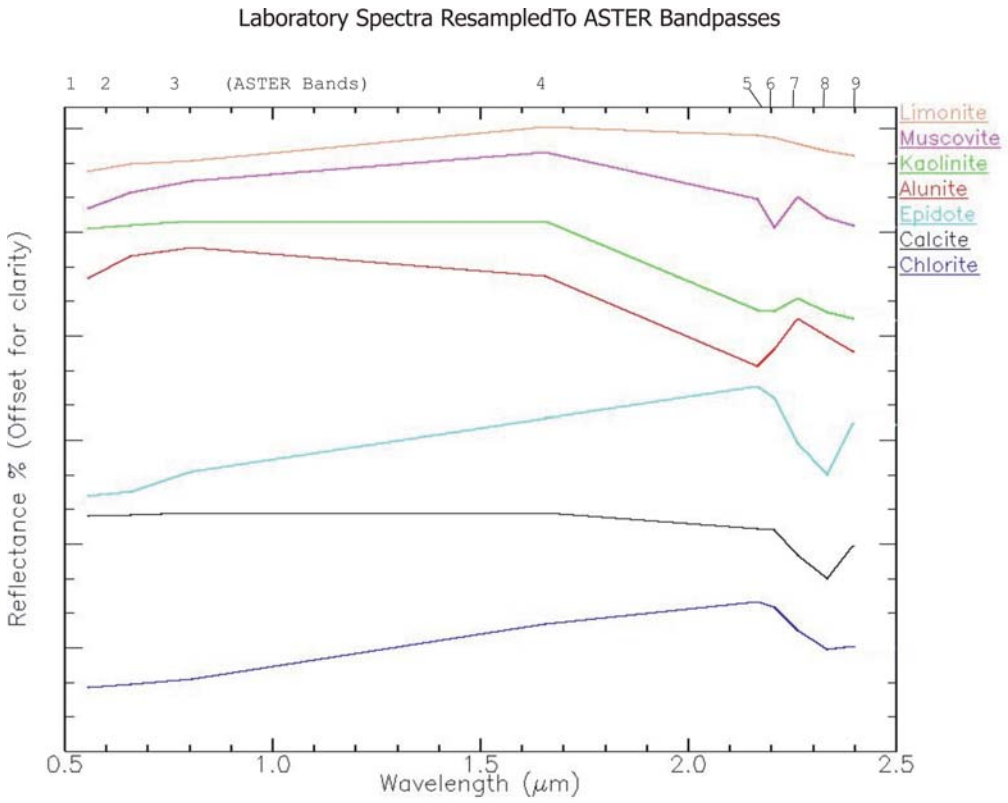

Figure 5. Laboratory spectra of limonite, muscovite, kaolinite, alunite, epidote, calcite, and chlorite resampled to ASTER bandpasses.
Spectra include limonite with a broad 0.66-1.1.65 µm absorption feature; muscovite typically in phyllic alteration, with a 2.20 µm absorption feature; kaolinite and alunite, which are common in argillic alteration feature; have 2.165 and 2.20 µm absorption feature; and epidote, calcite, and chlorite, which are typically associated with propylitic alteration and display 2.32, 2.33, and 2.32 µm absorption features respectively. Epidote and chlorite have a broad Fe2+ absorption feature that affects ASTER band 2, 3, and 4 (0.66-165 µm) (Clark et al., 1993b).

4.2 Advanced Spaceborne Thermal Emission and Reflection Radiometer (ASTER) System

The Advanced Spaceborne Thermal Emission and Reflection Radiometer (ASTER) is an advanced multi spectral imager that was launched on board NASA's Terra spacecraft in December, 1999 (Abrams, et al., 2002).

The Terra spacecraft is flaying in a circular, near-polar orbit on an altitude of 705 km. The orbit is sun-synchronous with equatorial crossing at local time of 10:30 a.m., returning to the same orbit every 16 days. The orbit parameters are the same as of Landsat 7, except for the local equatorial time (Abrams, et al., 2002). ASTER can

acquire data over the entire glob and each ASTER scene covers an area of 60 km by 60 km (Abrams, et al., 2002).

Table 5. The three ASTER sub system characteristics.

Subsystem	Band No.	Spectral Range (μm)	Spatial Resolution, m
VNIR	1	0.52-0.60	15
	2	0.63-0.69	
	3N	0.78-0.86	
	3B	0.78-0.86	
SWIR	4	1.60-1.70	30
	5	2.145-2.185	
	6	2.185-2.225	
	7	2.235-2.285	
	8	2.295-2.365	
	9	2.360-2.430	
TIR	10	8.125-8.475	90
	11	8.475-8.825	
	12	8.925-9.275	
	13	10.25-10.95	
	14	10.95-11.65	

The system consist three separate radiometers, namely: Visible and Near Infrared Radiometer (VNIR), Shortwave Infrared Radiometer (SWIR) and Thermal Inferred Radiometer (TIR). The subsystem characteristics are shown on Table 5.

ASTER instruments on board covers wide spectral region with 14 bands rang from visible region to thermal infrared with spatial, spectral and radiometric resolution. An additional backward-looking near infrared band provides stereo coverage. The spatial resolution varies with wavelength, 15 meter in Visible and Near-inferred (VNIR), 30 meter in the Shortwave Infrared (SWIR), and 90 meter in the Thermal (TIR).

The Aster spectral data consists of two levels, Level-A (L1A) and Level-1B (L1B). The level L1A data is unprocessed instrument data The L1B data are generated by applying different coefficient for radiometric calibration and geometric re-sampling on

L1A data. ASTER products are stored in a specific implementation of Hierarchical Data Format called HDF-EOS.

4.3 Spectral Signatures of Minerals

By spectral signature is meant a single feature or pattern of features whose shapes, locations, and relative intensities are characteristics of a particular material (Siegal, et al., 1980).

Remote sensing becomes a powerful mineral exploration tool, when the primary and secondary process of mineralization results in the formation of spectral anomalies. The features comprising the spectral signatures of minerals are produced as a consequence of either electronic or vibrational process. To occur, these two processes require different amount of energy, and thus evidence for their occurrence appears in different region of spectrum (Siegal, 1980). Those appear in the form of bands and slopes in the visible and far-infrared (0.325 to 2.5 μm) bi-directional reflection spectra of minerals. Rocks are assemblage of minerals, and so the spectrum of a rock is a composite of the individual spectra of its constituent minerals.

Spectral data collected from large number collection of minerals are used to generate a "Spectral Signature" diagrams showing the optimum fundamental spectra of particular minerals.

Major mineral constituents of rock, namely silicon, aluminum, magnesium and oxygen, do not produce absorption feature in the VNIR range. The most commonly observed features are due to the presence of iron as Ferric/Ferrous form, or the presence of water or OH groups (Hunt, 1977).

The typical spectra of iron oxides lies in the wavelength range of 0.35 to 1.5 μm. The occurrence of absorption anomalies at wave length less than 0.9 μm is a good indication that hematite is the predominant mineral. Anomalies found at wavelength closer or larger than 0.9 μm, suggest abundance of jarosite or goethite (Hunt and

Ashley, 1979). Figure 6 shows reflectance spectra of common iron-bearing minerals that display features resulting from electronic transition in ferrous (Fe^{2+}) ions.

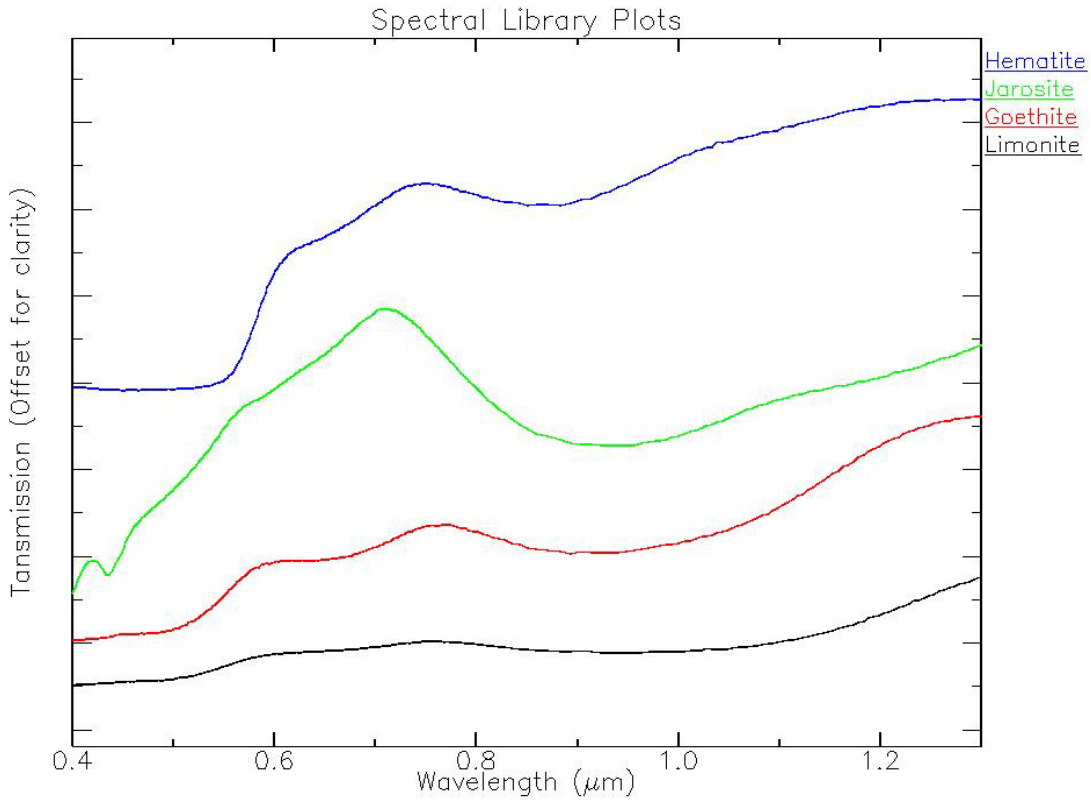

Figure 6. Spectra of common iron oxides and hydroxides bearing minerals. (Hunt and Salisbury, 1970b; 1971; Hunt, 1979)

Vibrational transitions produce reflectance anomalies in the near-infrared region of spectrum, between 1 and 2.5 μm, and they provide more information about mineralogical rock composition than the spectral features observed in the visible and near-infrared region.

In the SWIR part of the spectrum the most important vibrational transitions in mineral are those associated with the presence of OH ion or water molecules (Hunt and Ashley, 1979). Absorption features at 1.9, 1.4, 1.14 and 0.94 μm indicate the presence of molecular water in minerals. The bending of Al-OH and Mg-OH, producing distinctive absorption feature in the reflectance spectra, are prominent in aluminous mica and clay minerals (Fig. 7) and dominant signature of hydroxylated minerals that contain magnesium, such as talc and chlorite.

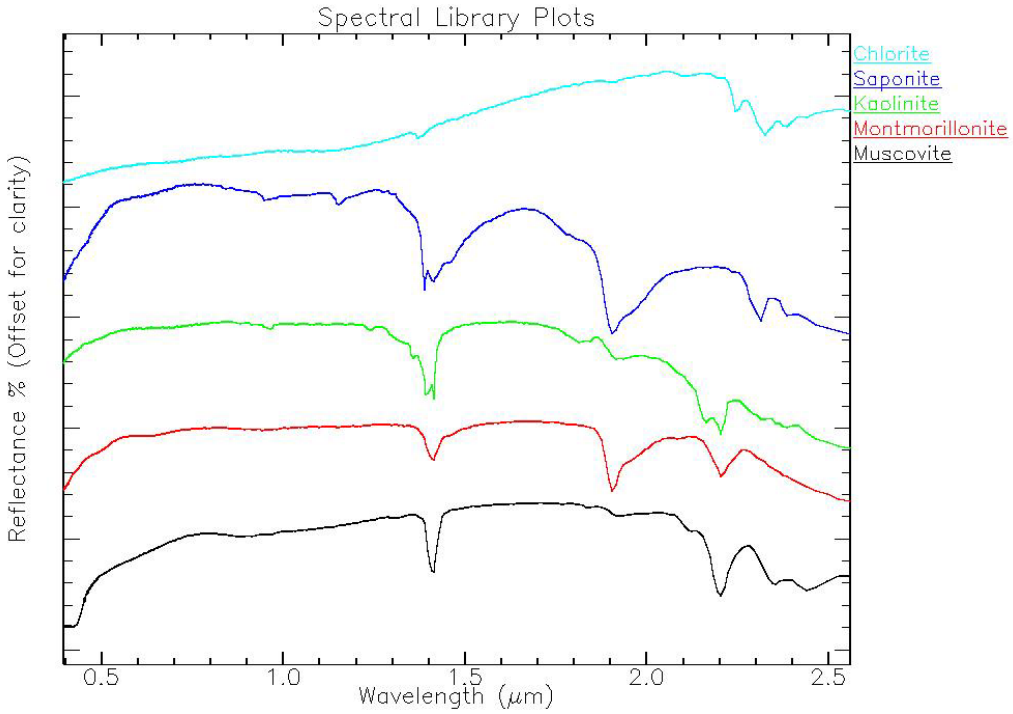

Figure 7. Spectra of clay minerals and mica.
(Hunt and Salisbury, 1970b; Hunt and Salisbury, 1971; Hunt, 1979)

Carbonates give rise to number of absorption features in the SWIR of which that around 2.3 μm most prominent (Fig. 8).

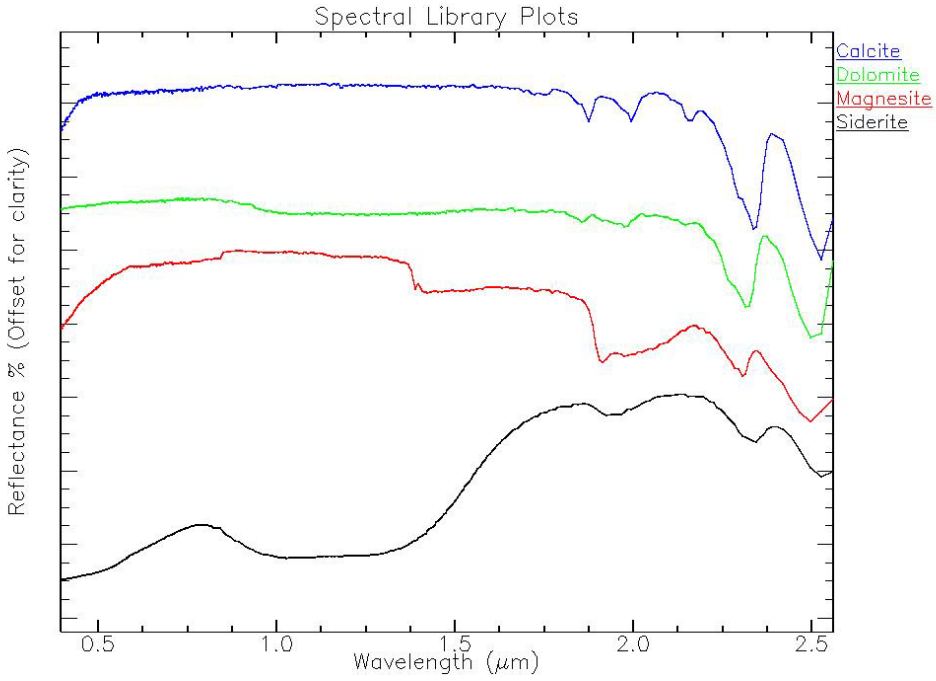

Figure 8. Spectra of common carbonate minerals.
(Hunt and Salisbury, 1970b; Hunt and Salisbury, 1971; Hunt, 1979)

5. RESULTS

5.1 GEOLOGICAL MAPPING

5.1.1 Enhanced False-Color Composite

Enhanced false color composite provides a good overview of the study area in color scheme that is most familiar and close to natural (Fig. 9). Lithologic and structural information is generally well contained in many of the high ranking band combinations. Band composite 8, 3 and 1 in R, G and B contains the maximum information (see Table 4). The contrast between the different lithologic units were also apparently enhanced in band composite 8, 4 and 2, in R, G and B respectively, which is a low ranking band combination but selected by visual inspection of various band composite possible from ASTER VNIR and SWIR data. Both images were used for lithological discrimination and extract structural information. Histogram equalization stretching of these images yield best enhanced product for visual interpretation, "Histogram equalization" is the process of redistributing pixel values so that there are approximately the same numbers of pixels with each value with in a range (ERDAS, 1982).

On band composite 8, 3 and 1 the hornblende-biotite gneiss and meta-gabbroic intrusive units appears as light magenta color. Examination of grey image of each band exhibited high reflection in band 8 and 1 and strong absorption in band 3. This suggests that absorption in band 3 probably attributed to alteration of iron contained in the mineralogical structure of biotite and hornblende. The high reflectance in band 8 is might resulted due to the absence of hydroxylated minerals.

Metagranite, Paleozoic sediment and Biotite-feldspar-quartz gneiss are in pink color resulted from overall high reflectance in band 8 and low reflectance in band 3 and 1.

At the northeast part of the area the Biotite-feldspar-quartz gneiss appears deep green, the Tertiary basalt appears yellowish green and the Biotite gneiss appear as

greenish cyan. This green dominant color mainly attributed to dense vegetation cover and the lithologic units at this part of the study area were distinguished in the processed image only by their slight difference in color and differences in their surface morphological appearance and field visit help the interpreted result.

The metasediments at the southeastern of the study area appears bleached (white) washed surface because of high reflectance in both three bands (8, 3 and 1) of the composite. The filed visit confirms the unit around Kemashi town hydrothermal altered and the alteration minerals spectral responses in the reference reflectance curves show high reflectance.

The metavolcanics unit at the southwest part of the area occupies undulating narrow hill and distinguished by its greenish blue color due to high reflectance in band 3 and 1 and strong absorption in band 8. The field observations confirm the unit is highly chloritized and epidotized and this are common hydrothermal alteration minerals have an iron and magnesium hydroxyl absorption feature at 2.35 μm (ASTER band 8).

The metavolcano-sediments appear green tinted grey colored and are characterized by irregularly distributed white and red spikes.

On this image, the Tertiary basalt, except crop out at the northeast of the area, appears dark because it has low reflectance in all three bands and is distinguished by its smooth morphology. The Tertiary trachyte unit mapped at a few places and appears as bright color and distinguished by its small circular morphology.

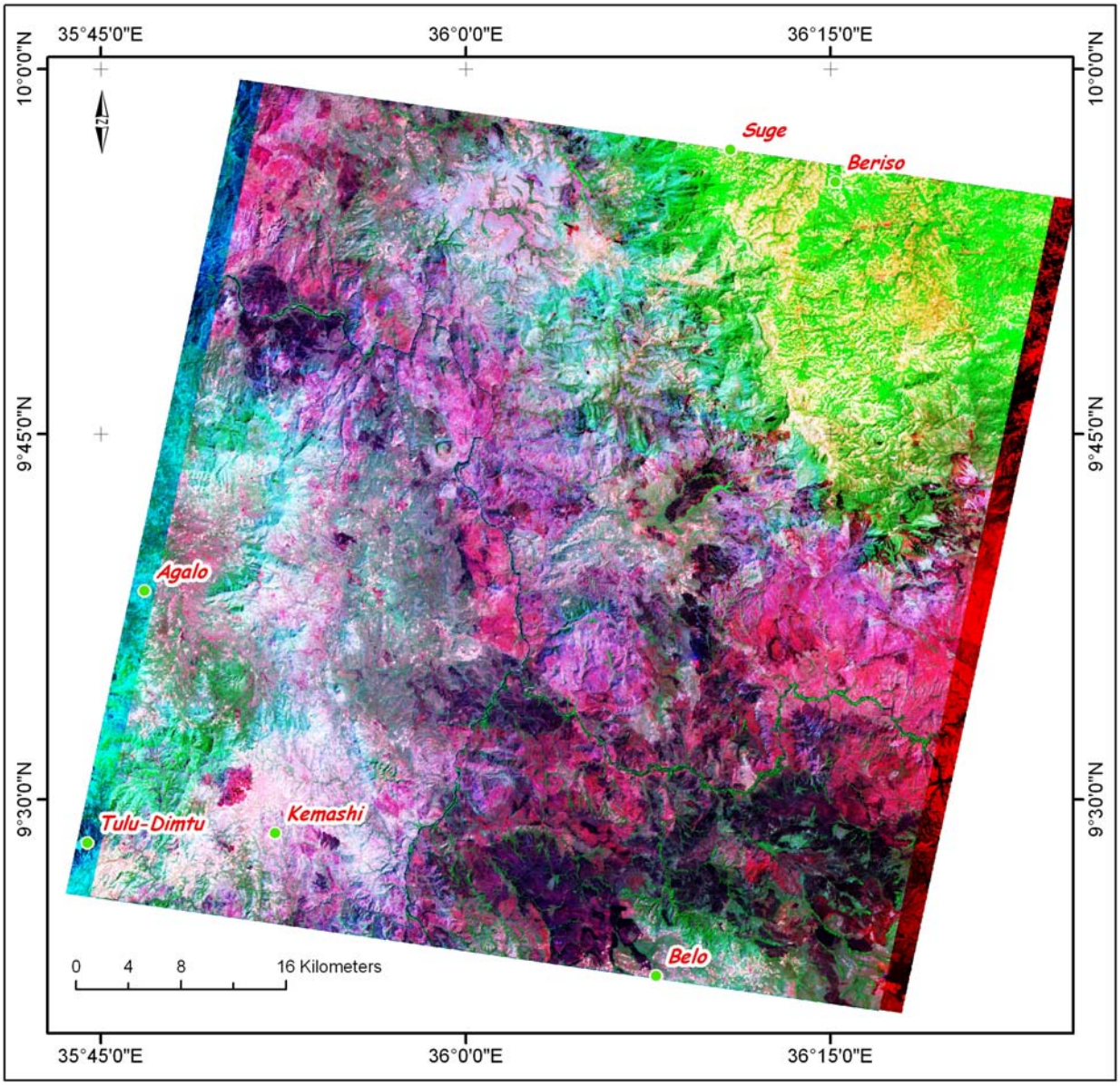

Figure 9. Enhanced false color composite image of ASTER band 8, 3 and 1 in R, G and B, respectively obtained for the study area.

5.1.2 Intensity-Hue-Saturation (IHS) Transformation

IHS transformation was applied to ASTER band 8, 3, and 1. For contrast enhancement saturation and intensity images stretched separately and both intensity and saturation stretched simultaneously by keeping hue image unchanged in both transformations. In both transformations the different lithological units have similar color as in the false color composite of ASTER band 8, 3, and 1 with insignificant saturation and intensity improvement.

5.1.3 Principal Component Analysis (PCA)

In this study, PCA was performed on 9 bands covering VNIR and SWIR. The eigenvector and eigenvalue used for the transformation is shown in Table 6.

Table 6. Eigenvector statistics for ASTER 9 band (VNIR & SWIR).

Eigen-vector	PC1	PC2	PC3	PC4	PC5	PC6	PC7	PC8	PC9
Aster_1	0.2873	-0.1930	0.5339	-0.0979	0.6601	-0.2742	0.2659	0.0524	-0.0362
Aster_2	0.4116	-0.2323	0.6035	-0.0283	-0.5821	0.1956	-0.1720	-0.0632	0.0312
Aster_3	0.3441	0.8343	0.0642	-0.4082	0.0456	0.0816	-0.0752	0.0133	0.0124
Aster_4	0.4987	0.2114	-0.1769	0.7276	-0.0848	-0.0999	0.3414	-0.0500	-0.0988
Aster_5	0.2878	-0.1248	-0.2023	0.0326	0.2150	-0.2209	-0.6486	-0.5733	-0.1236
Aster_6	0.3459	-0.1698	-0.2313	0.0516	0.1529	0.1068	-0.4164	0.7576	0.1152
Aster_7	0.2729	-0.2063	-0.2655	-0.1702	0.1401	0.4256	0.2625	-0.2844	0.6580
Aster_8	0.2560	-0.2519	-0.2958	-0.3628	-0.0263	0.2926	0.2760	-0.0169	-0.6994
Aster_9	0.1960	-0.1325	-0.2510	-0.3596	-0.3555	-0.7368	0.1961	0.0827	0.1926
Eigen-value	458.11	109.879	48.459	12.1495	2.5718	1.2441	1.078	0.7955	0.66194
Variance (%)	72.149	17.3051	7.6319	1.91346	0.405	0.1959	0.1698	0.1253	0.10425

PC 1, with 72% variance and positive loading from all ASTER bands, contains significant albedo and topographic information and that accounts for high correlation between the input bands. PC1, PC2, PC3 and PC4 display fair lithologic contrast and the rest of the PC (PC5 to PC9) show strips and noisy images and appear to be less informative. RGB composite of PC1, PC2 and PC3 have better color contrast and allowed best lithologic discrimination (Fig. 10). Histogram equalization of this composite improved the color saturation.

On this composite PC image Tertiary basalt display as blue color and in most part of the area it is distinctly mapped. In the south part of the area both the hornblende-biotite gneiss and the Tertiary basalt appear blue and difficult to discriminate. The raw data color composite (8, 3, & 1) offered good contrast to discriminate the two lithologies in this particular area.

In this image hornblende-biotite gneiss and basic intrusives appear as blue tinted magenta color. The metasediments appears as light magenta color. Metagranite and Biotite-feldspar-quartz gneiss appear pinkish color. The metavolcanics at the

southwest of the area and the Biotite gneiss at the northern part of the area show light blue color. The Paleozoic sedimentary units and the Tertiary basalt at the northeast corner of the area appear yellowish and distinct from the Biotite-feldspar-quartz gneiss that is in contact. The strip of the Tertiary basalt in this part of the study area also discriminated by its rough image texture. The high positive loading of band 3 in PC2 is due to the dense vegetation cover and account for green color in most lithologic units.

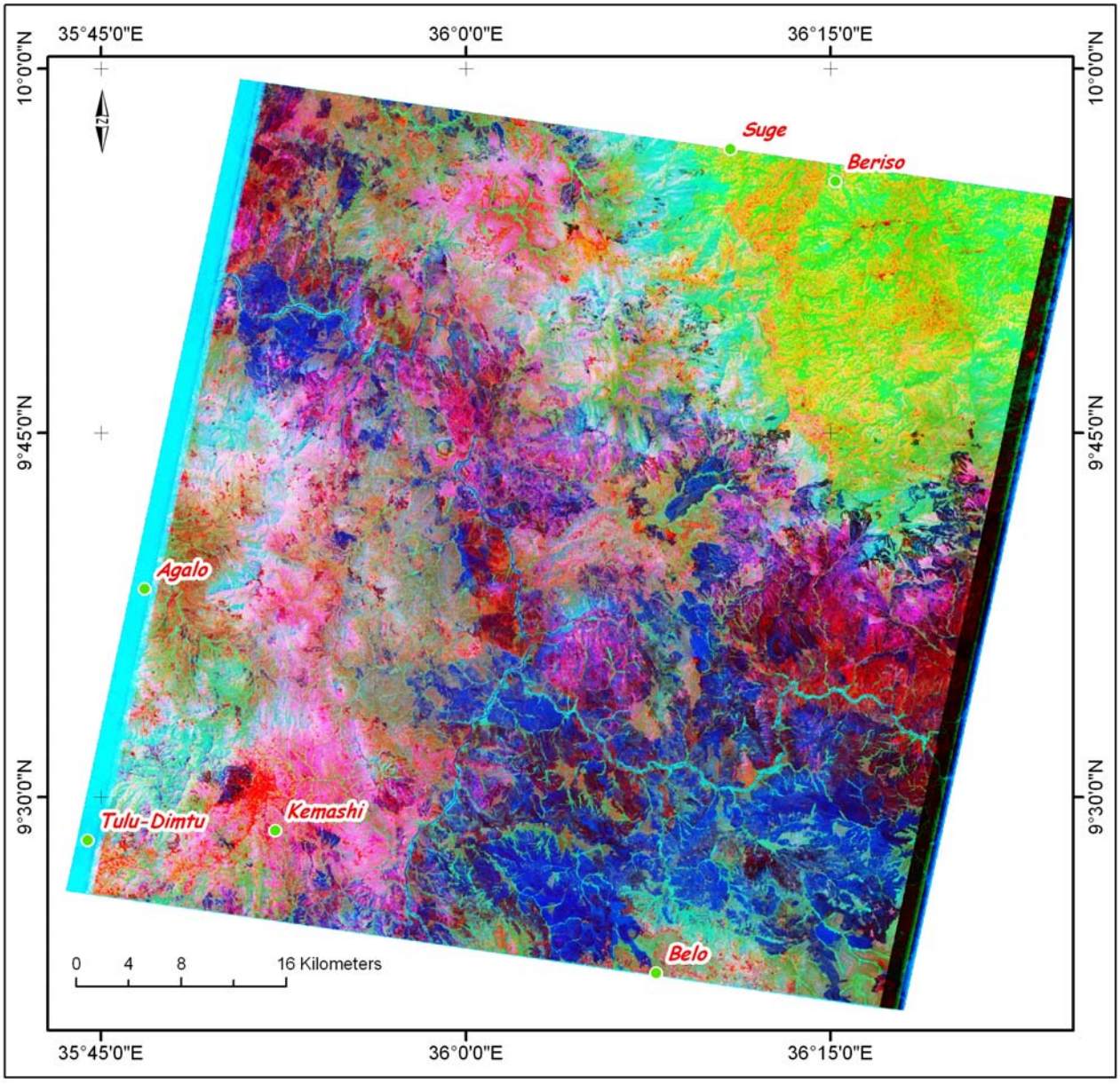

Figure 10. RGB color composite of PCA 1, 2 & 3 of the study area.

During the image interpretation different lithologies have been considered as a unit when among others they are primarily characterized by distinctive and substantially homogenous spectral responses, consist dominantly of one lithologic type or combination of types, have easily recognizable geologic boundaries, and are large enough to represent on the geological map at a desired scale of 1:125,000. In addition to the above interpreted images, which are bases for interpretation, additional information also was used from images obtained from other enhancement techniques. Thirteen lithologic units were interpreted in the processed images and these are: Quaternary sediment, Tertiary trachyte, Tertiary basalt, Paleozoic sediments, Metagranite, Metagabbro, Metaultramafic, Metasediments, Metavolcanics, Metavolcano-sediments, Hornblende-biotite gneiss, Biotite gneiss, and Biotite-feldspar-quartz gneiss. The obtained geological interpretation map of the study area is shown on figure 11.

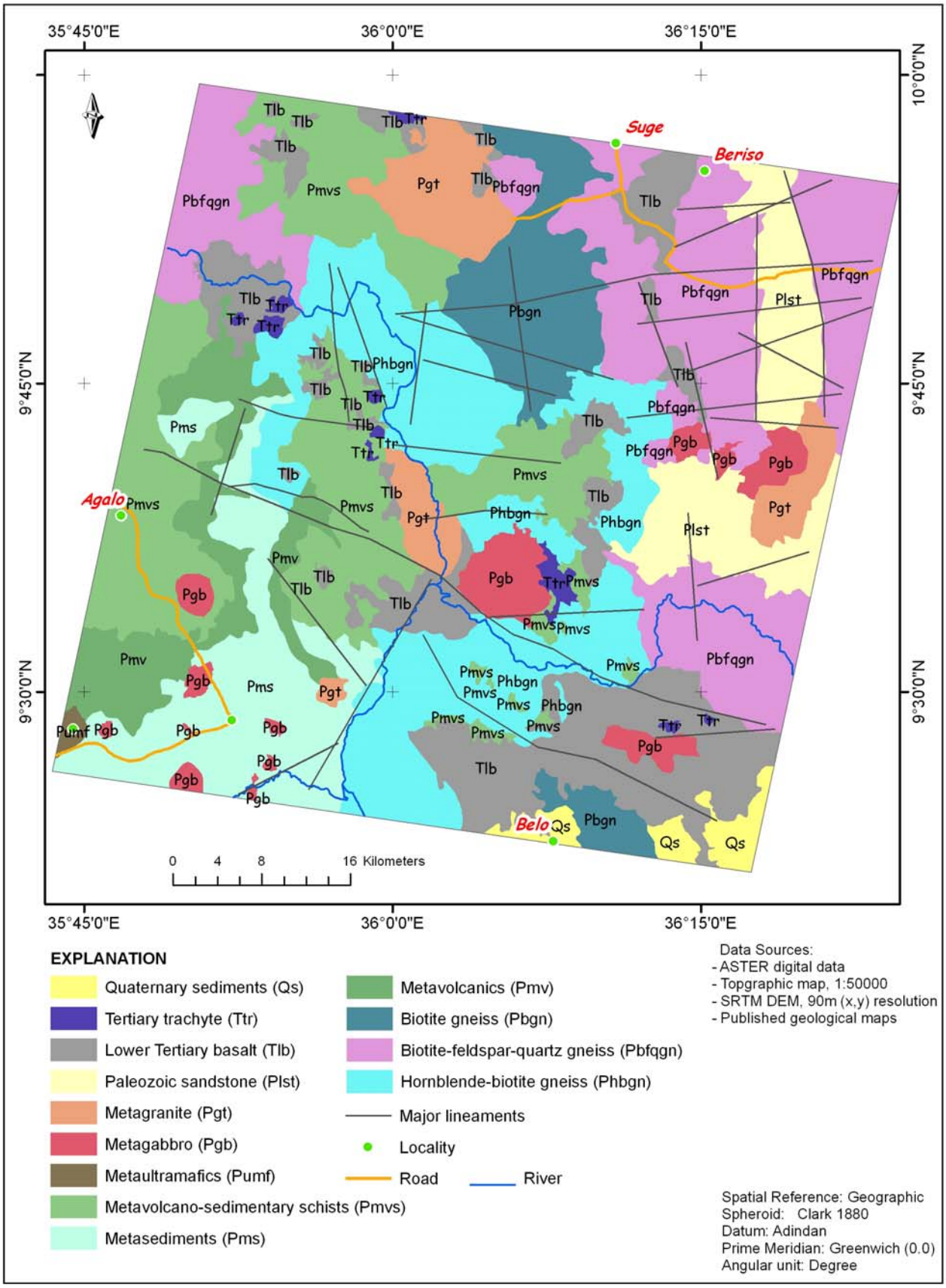

Figure 11. A Geological interpretation map of the study area.

5.2 LINEAMENT MAPPING

A lineament is mappable, simple or composite linear feature of a surface, whose part are aligned in rectilinear or slightly curvilinear relationship and which differ distinctly from the patterns of adjacent features and presumably reflects a subsurface phenomenon (O' Leary et al., 1976).

The term was introduced by different geological workers and agree on the following general properties: (1) lineaments have geomorphic expression, in general topographically negative, (2) lineaments are composite (either segmented or complex), (3) are characterized by alignment in a single direction, which may or may not conform to regional trend, (4) are straight or slightly curved, (5) are regional in extent, and are scale related.

Mapping of lineament or structural features of any region may provide useful information for mineral exploration studies. Similarly, lineament analysis techniques using remote sensed data help researchers to identify different structural regimes and mineralized zones (Rowan and Bowers, 1995).

For this study several image processing and enhancement techniques including: directional filtering, PCA, hill-shading of DEM and band rationing have been used to enhance structural features. Lineaments were visually interpreted by excluding man-made features such as road, foot path, and farming plots divide.

5.2.1 Convolution Filtering

For the purpose of lineament analyses spatial enhancement were performed using directional filters. Directional filters are quite useful for producing artificial effects which may reveal tectonically controlled linear features (Drury, 1986).

In order to aid visual interpretation, different convolution filters of variable window size were applied. For the purpose of smaller and medium size lineament identification the mid-low filters of 3x3 windows, which are commonly used edge detection filters known as *Gradient-Soble* and *Gradient-Prewitt,* provide the best improvement. The larger lineaments are preferably enhanced by using 7x7 widow size directional filters adapted from Kenea, 1997. The directional filters (NS, EW NE and NW) were chosen based on the structural features of the region and applied to ASTER band 4, it is chosen because all ground features has relatively high reflectance in this band. The four principal directional filters are given in Table 7 & 8.

Table 7. 7x7 window size filters in the four main directions applied in the study.

N-S							**E-W**						
1	1	1	1	1	1	1	1	1	1	1	-1	-1	-1
1	1	1	1	1	1	1	1	1	1	1	-1	-1	-1
1	1	1	1	1	1	1	1	1	1	1	-1	-1	-1
1	1	1	-2	1	1	1	1	1	1	-2	-1	-1	-1
-1	-1	-1	-1	-1	-1	-1	1	1	1	1	-1	-1	-1
-1	-1	-1	-1	-1	-1	-1	1	1	1	1	-1	-1	-1
-1	-1	-1	-1	-1	-1	-1	1	1	1	1	-1	-1	-1
NE-SW							**NW-SE**						
1	1	1	1	1	1	1	1	1	1	1	1	1	1
-1	1	1	1	1	1	1	1	1	1	1	1	1	-1
-1	-1	1	1	1	1	1	1	1	1	1	1	-1	-1
-1	-1	-1	-2	1	1	1	1	1	1	-2	-1	-1	-1
-1	-1	-1	-1	1	1	1	1	1	1	-1	-1	-1	-1
-1	-1	-1	-1	-1	1	1	1	1	-1	-1	-1	-1	-1
-1	-1	-1	-1	-1	-1	1	1	-1	-1	-1	-1	-1	-1

Table 8. 3x3 window size filters in the four main directions applied in the study.

	N-S			E-W			NE-SW			NW-SE		
SOBLE	-1	0	1	-1	-2	-1	-2	-1	0	0	1	2
	-2	0	2	0	0	0	-1	0	1	-1	0	1
	-1	0	1	1	2	1	0	1	2	-2	-1	0
PREWITT	-1	0	1	-1	-1	-1	-1	-1	0	0	1	1
	-1	0	1	0	0	0	-1	0	1	-1	0	1
	-1	0	1	1	1	1	0	1	1	-1	-1	0

Some of the results of the 3x3 and 7x7 window filters are given in Figure 12, for the two main directions (NE and NW). These figures belong to small section in the study area to show the details of the result obtained.

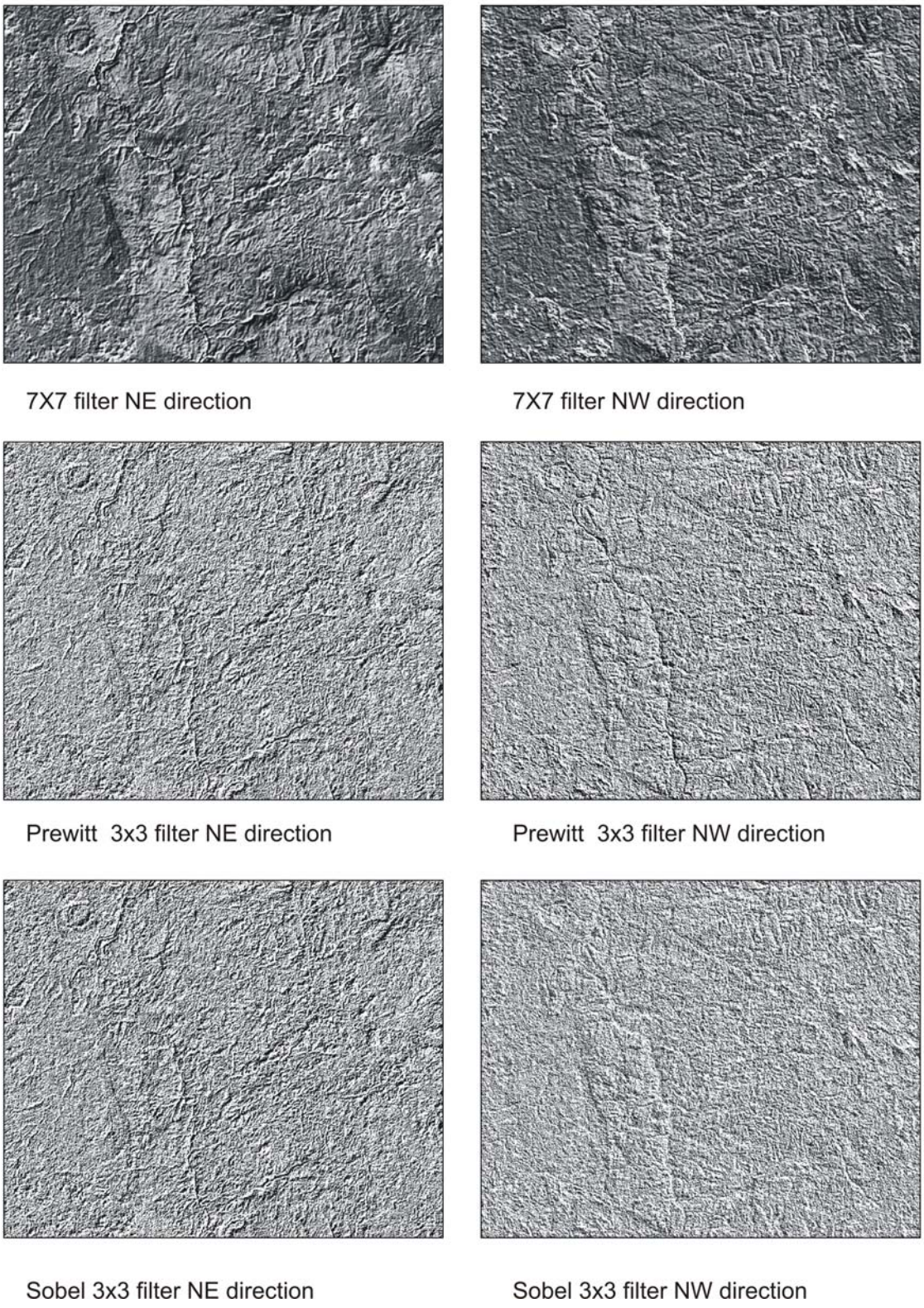

Figure 12. 3x3 and 7X7 window size filtered images in NE and NW direction.

5.2.2 Digital Elevation Model (DEM)

Lineament analysis in this study also primarily based on the interpretation of SRTM DEM. The primary method used for the lineament interpretation using SRTM DEM was through the creation of hill-shade DEM, this technique is effective in creating images that enhance geomorphologic features. Hill-shades DEM with different azimuth direction and sun angle were used in this study (Fig. 13).

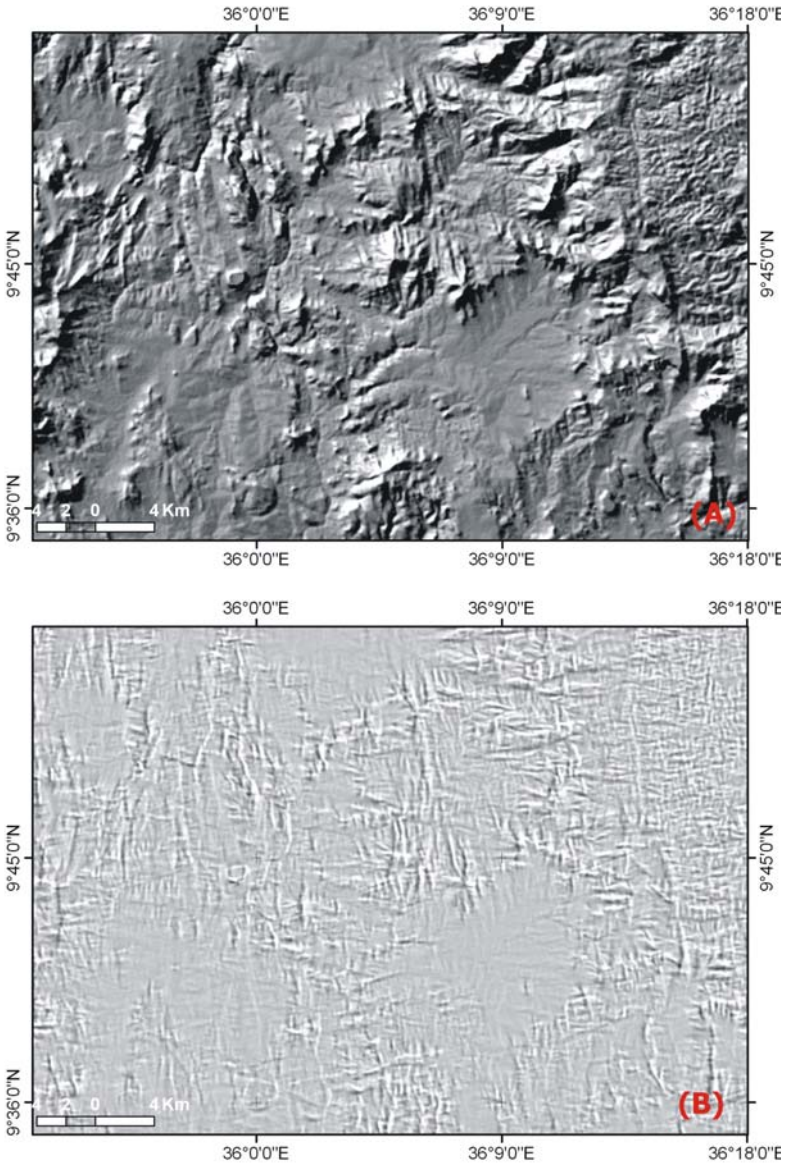

Figure 13. SRTM hill-shading image for the sub-set of the study area.
(A) illuminated from a 315° azimuth direction and a 45° false sun angle, and (B) illuminated from a 45° azimuth direction and a 10° false sun angle, sub-set of the study area.

5.2.3 Lineaments Interpretation

Lineaments were visually interpreted from the enhanced images and where lineaments well over 1 km long were manually traced. The width of the lineaments in the interpreted images are various but not considered for lineament analysis. In the study area a total of 1105 lineaments were recognized and analyzed. The interpreted lineament map of the area is shown in figure 14.

To summarize and analyze the lineaments in the study area a rose diagram for the total lineaments were prepared, which is a polar plots of direction verses frequency of the lineaments (Fig. 15). The rose diagram indict the lineaments are highly dispersed. The mean lineament orientation in the study area is in the NNW direction.

For close observation and interpretation of structures a subset area were selected based on the occurrence of most of the regional structures in relatively closer range. Raw ASTER data color composite, PC color composite and Hill-shade image were used for the interpretation (Fig. 16 A, B & C).

In the subset maps three major regional structural elements were recognized namely: foliation, folds and lineament (fault or fracture) (Fig. 16 D). Foliations are penetrative and recognized in most of the metamorphic lithologic units, with NE and NW trending directions.

The major fold in the subset maps is the most prominent structure and covers the entire sub area. It is a tight fold and the axial trace run NNW with slight undulation and extends for about 16 km.

Lineament (fault/fracture) with three major directions, NE, NW, and EW orientations, are clearly identified in the sub area maps.

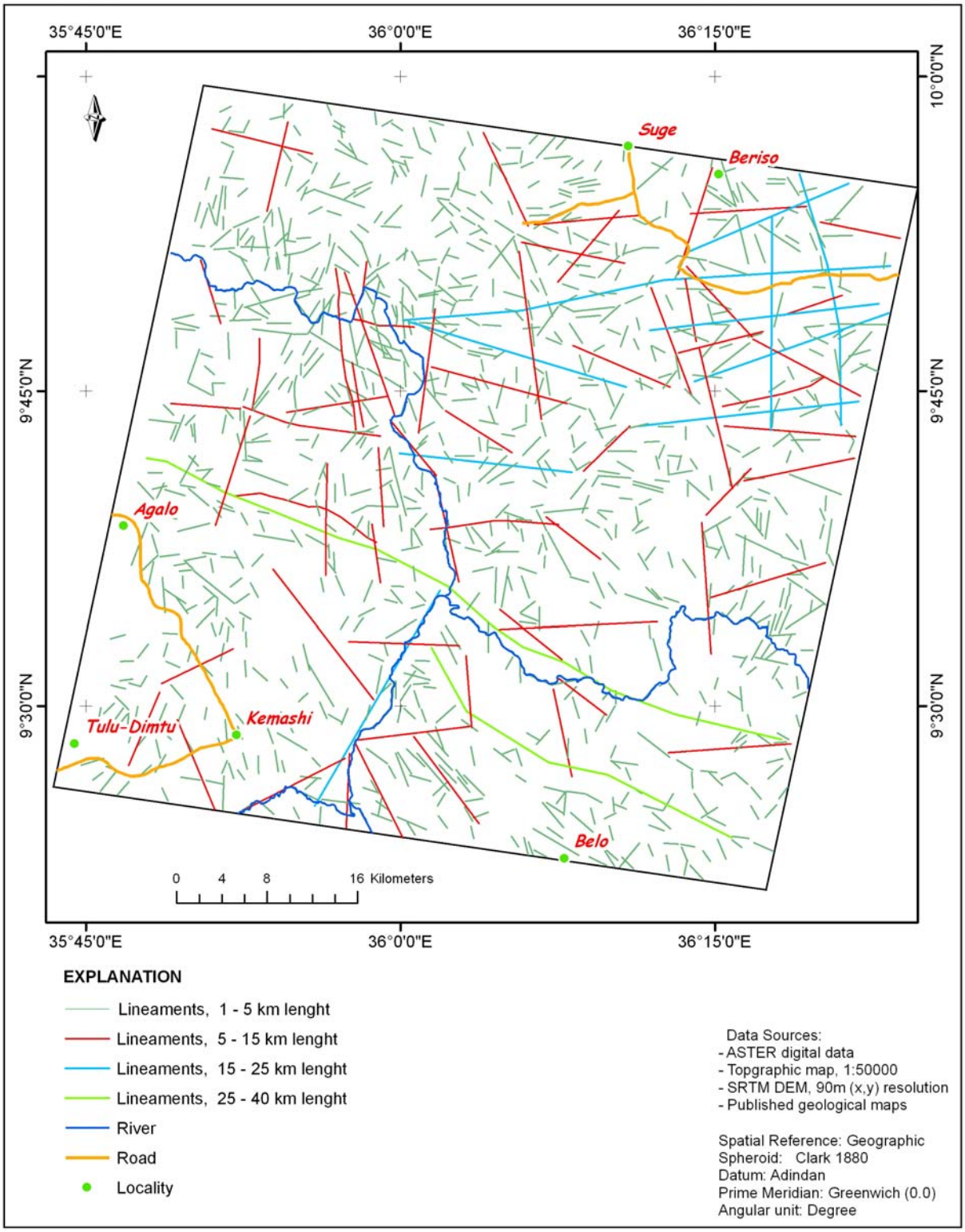

Figure 14. A Lineament interpreted map of the study area.

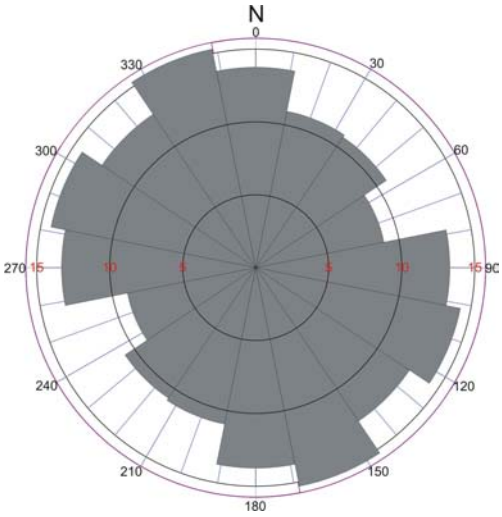

Figure 15. Rose diagram plot of all 1105 lineaments in the study area.

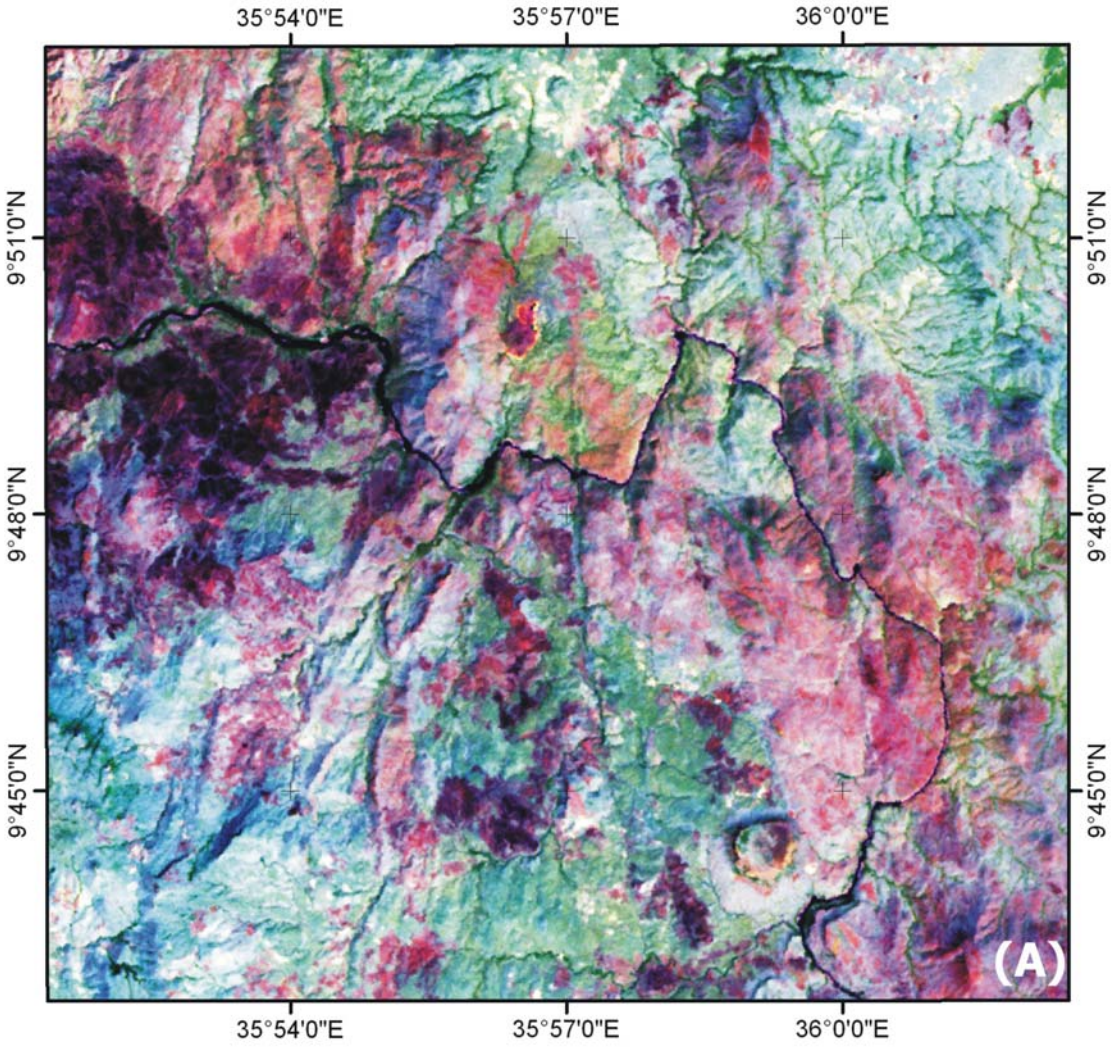

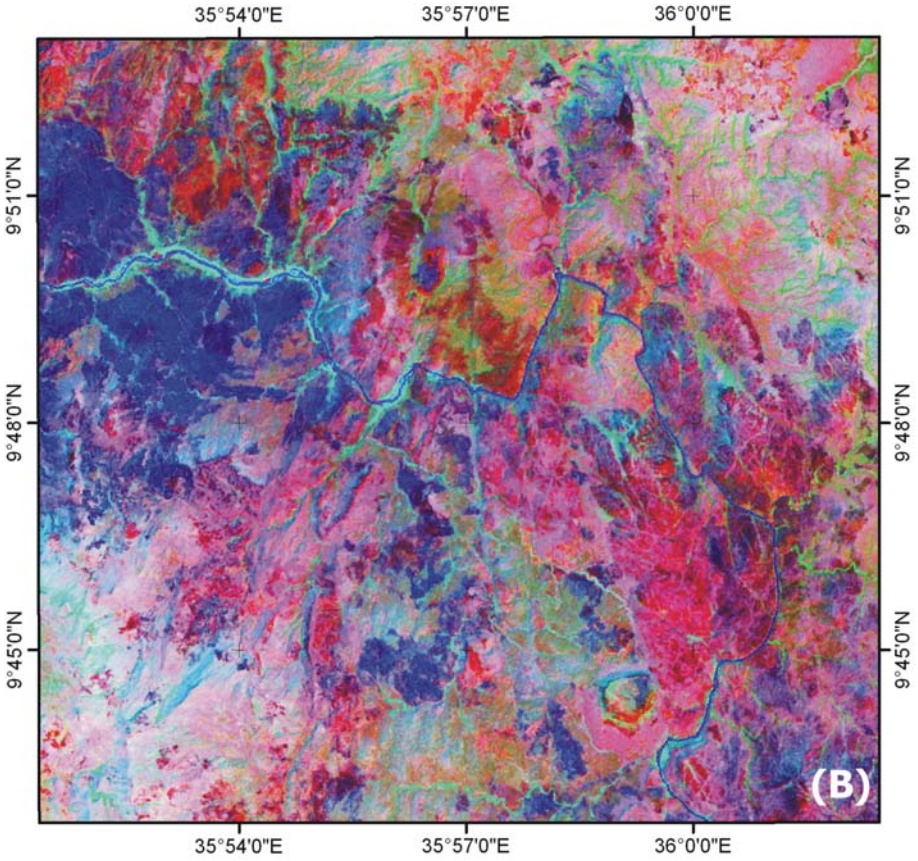
35°54'0"E
35°57'0"E
36°0'0"E
9°51'0"N
9°48'0"N
9°45'0"N
(B)

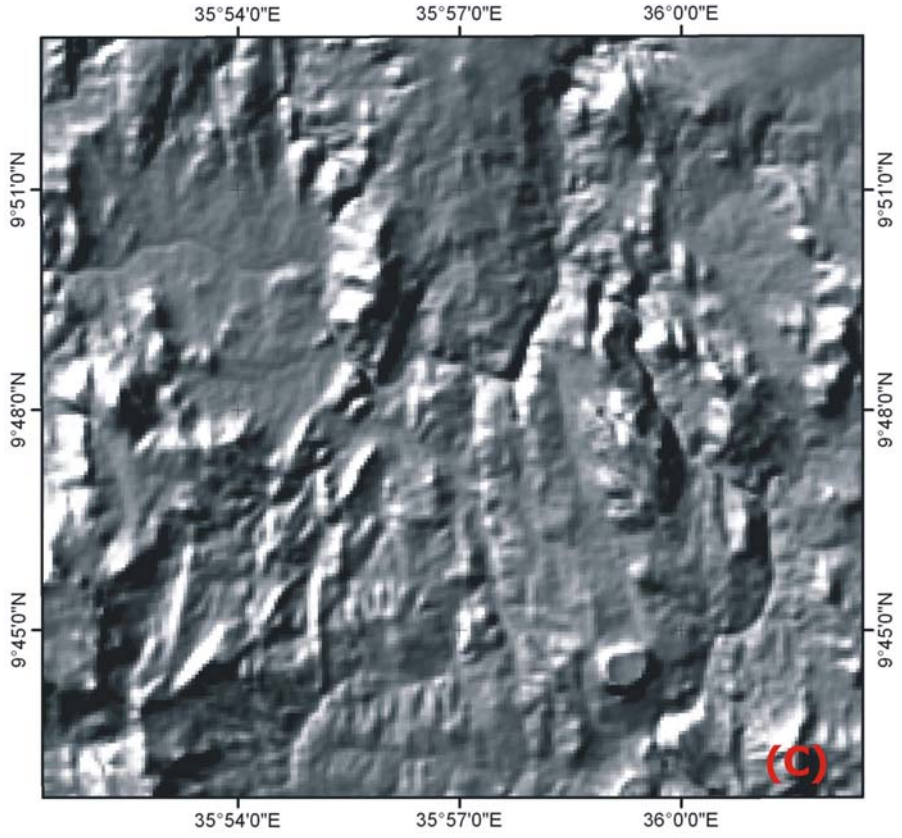
35°54'0"E
35°57'0"E
36°0'0"E
9°51'0"N
9°48'0"N
9°45'0"N
(C)

"Z" shaped small folds on both limbs of the major fold were observed, this folds could be resulted from the progressive deformation of D2 event or related to the D3 shear structure reported in the published geological map. Anger-Diddesa river channel follow the different structures in the sub area.

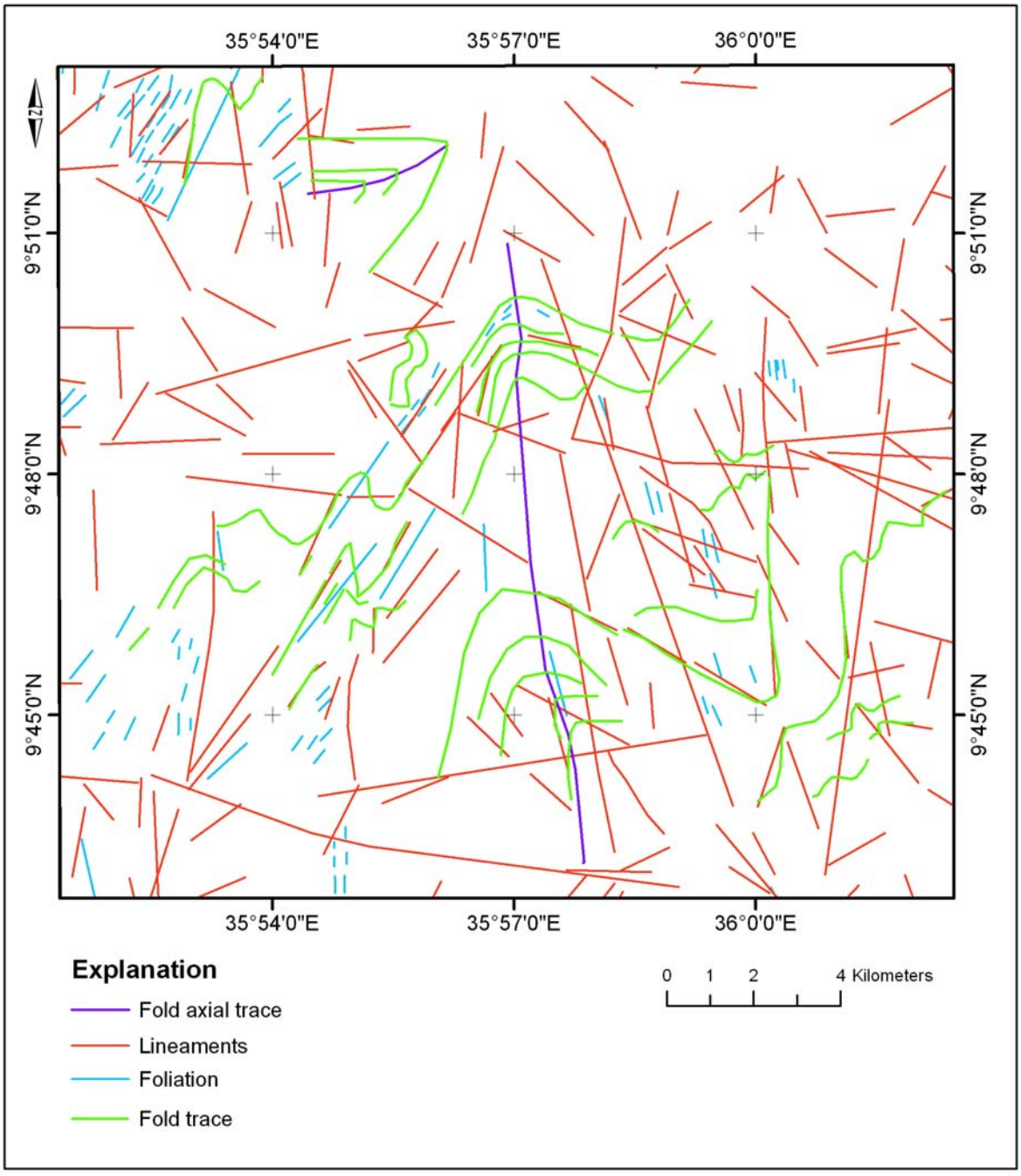

Figure 16. Detail structural interpretation in small section of the study area.
(A) False color composite of ASTER band 8, 3 & 1 (B) PC color composite (C) Hill-shade of the sub area. (D) Interpreted structural elements in the sub set area.

5.3 HYDROTHERMAL ALTERATION MAPPING

Hydrothermal alteration, referred as wall-rock alteration, is a general term that encompasses many processes by which rock-forming minerals are altered due to reactions accompanying the flow of heated aqueous fluids along fractures and grain boundaries (Meyer and Hemley, 1967 and Rose and Burt, 1979).

There is no ideal classification scheme for mineral alteration due to the extreme variability of the original mineralogy and the wide variety of conditions, which can exist in the hydrothermal alteration environment. Below is a summary of most widely recognized alteration types:

Potassic Alteration: results in the enrichment of potassium in the rock. The mineral commonly formed includes potassium feldspar, biotite and sericite.
Sodic Alteration: result in the enrichment of sodium in the rock.
Silicification: involves the addition of silica (SiO_2). In most case the addition of quartz.
Propylitic Alteration: generally involve the introduction of chlorite, which often causes rocks to take on greenish appearance.
Argillic Alteration: involves the introduction of clay minerals, the most common being clay mineral kaolinite. It forms most often at shallow depth.
Carbonate Alteration: which forms carbonate minerals such as calcite, ankerite and sederite.
Sericitic (Phyllic) Alteration: as the name implies, involves the formation of the mineral sericite, although it includes the formation of several different species of fine-grained white mica.

Alteration minerals that form a chemically stable assemblage will make an "alteration zone" or "halo" and the predominant mineral with in an assemblage is often used to indicate the intensive replacement. Assemblages are also named for group of minerals (Guilbert and Park, 1986).

Alteration zoning must be thought of in all three dimensions, i.e., both aerial distribution and depth. If the fluids migrate from the center outward from spherical source through homogenous (same throughout) rock, they would tend to form concentric shell. If they migrate outward from fissure, they would tend to form parallel bands or layers.

Most ore deposits have some type of recognizable alteration zoning pattern. Figure 19 illustrates hydrothermal alteration zones, minerals, and ore in a Porphyry Copper Deposit (modified from Lowell and Guilbert, 1970).

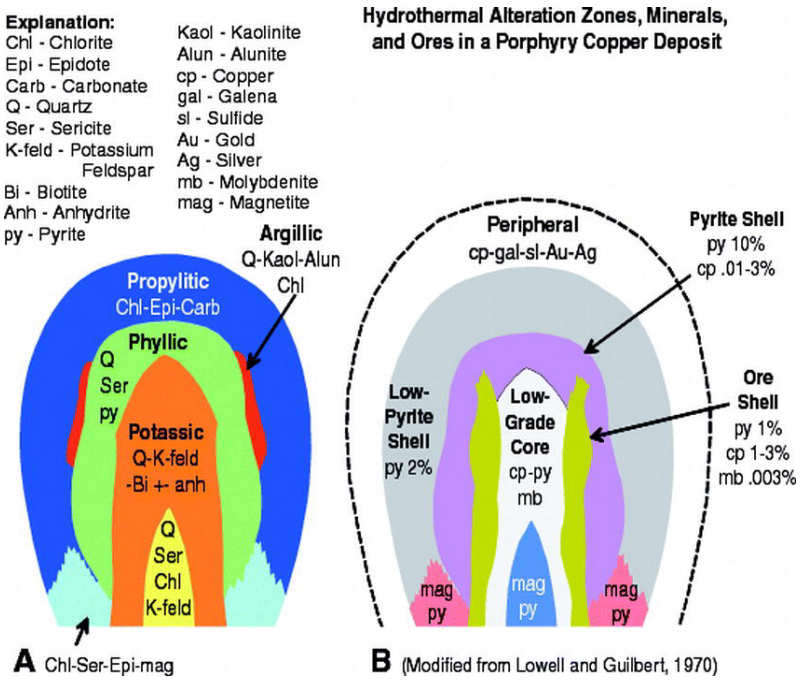

Figure 17. Classical alteration model of porphyry cooper deposit.
(Modified from Lowell and Guilbert, 1970). (A) Schematic cross section of hydrothermal alteration minerals and types, which include propylitic, argillic, and potassic alteration. (B) Schematic cross section of ores associated with each alteration type.

Since most mineral occurrences involves some or all alterations including iron oxide and hydroxyl-bearing minerals their detection has been used for many exploration projects. One of the purposes of this study is to map hydrothermally altered rocks at a regional scale using band rationing and feature oriented principal component analysis methods applied on ASTER multispectral data.

5.3.1 Alteration Mapping Using Ratio Images

For this study Argillic, Phyllic and Iron oxide/hydroxide hydrothermal alteration mapping were conducted using ASTER bands ratio. Multiple ratios and band thresholds were applied to a scene using algorithm (Fig. 18) developed by Mars et al., 2006. The authors used band ratios 4/5, 4/6, 5/6 and 7/6, which define the 2.17 μm and 2.2 μm absorption features, to map argillic and phyllic altered rocks.

The algorithm performs a series of band ratios. Each operator determines a true or false value for each ratio by comparing the band ratio to a predetermined range of threshold values. All of the ratios in the algorithm have to be true in order for a value of "1" to be assigned to the byte image; otherwise a "0" value is produced. Thus, a byte image consisting of zeros and ones is produced with each algorithm. The algorithm developer calibrate the ASTER seen using known and pre-studied site of hydrothermal alteration, and laboratory spectra were resampled to ASTER bandpasses (Fig. 19) and spectroscopically assessed to determine the range of ratios and band DN values to constrain the algorithm.

5.3.1.1 Argillic Band Ratio

The first part of the argillic band ratio algorithm performs a band 3/2 ratio in order to mask out green vegetation (Fig. 18). A spectral analysis of image and laboratory spectra suggests that band 3/2-ratio threshold value of 1.35 and less typically constitute area that lack green vegetation (Mars, et al., 2006).

A spectral analysis of ASTER image spectra and resampled ASTER laboratory spectra showed that band ratio 4/5, 5/6, and 7/6 were needed to map the 2.17 and 2.22 absorption features there by delineating argillic and phyllic altered rock (Figs. 18A & 19). Band ratios 4/5 and 4/6 map the 2.165 and 2.2 absorption features, respectively.

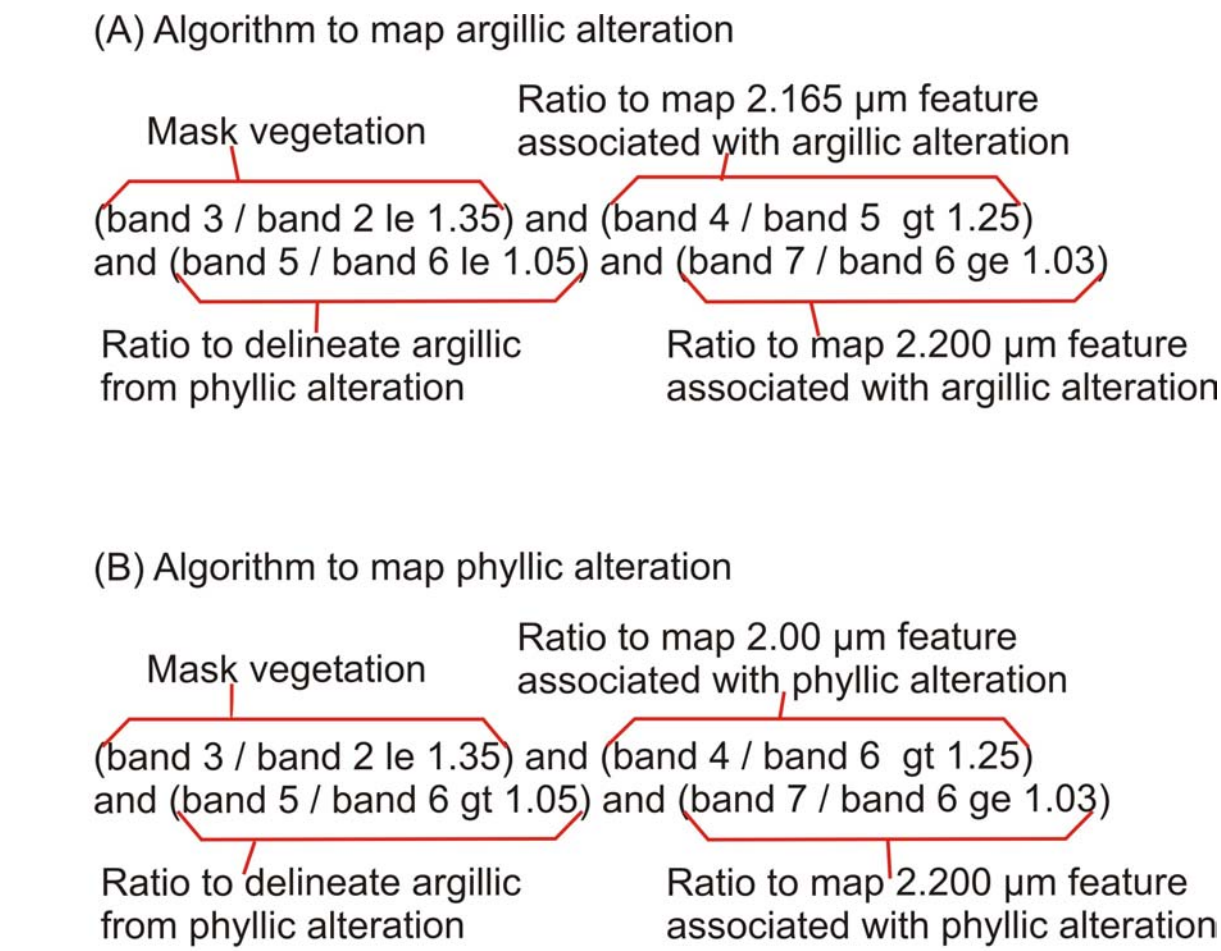

Figure 18. Algorithms that map argillic- and phyllic- altered rocks.
(A) Maps argillic-altered rocks using band ratios 4/5, 5/6, and 7/6, which define the 2.17 µm absorption feature. (B) Maps phyllic-altered rocks using band ratios 4/6, 5/6, and 7/6, which define the 2.20 µm absorption feature. Pixels with green vegetation are masked in the argillic and phyllic algorithms using band ratio of 3/2 (Marse et al., 2006).

Spectral analysis of ASTER spectra indicate that band 5 must be at least 5% lower than band 6 in order to map as argillic-altered rock; thus, the 5/6 band ratio delineates argillic from phyllic rock by classing ratio value 1.05 and less as argillic alteration (Figs. 18A & 19).

ASTER spectra of argillic-altered rock also illustrate that band 4 is at least 25% greater than band 5 and band 7 is 3% greater than band 6. Hence, values for band ratio 4/5 and 7/6 must be greater than 1.25 and greater than or equal to 1.03 respectively, to classify a pixel as argillic alteration (Fig. 18A).

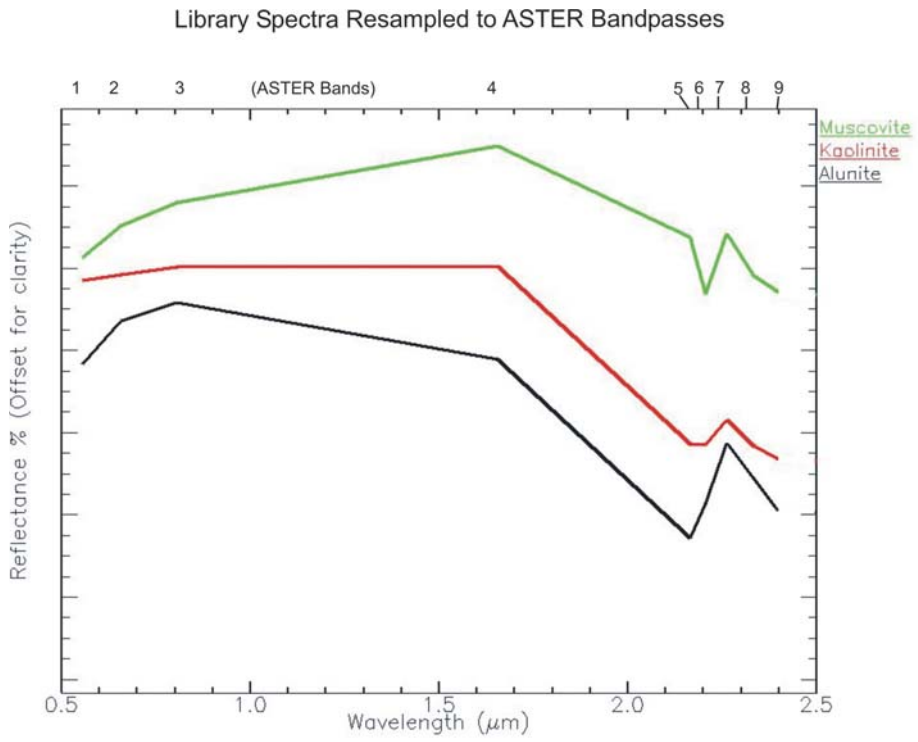

Figure 19. Laboratory spectra of muscovite, kaolinite, and alunite resampled to ASTER bandpasses.

The spectra intensities of absorption features in the 2.0-2.5 μm region used to define ratios in argillic and phyllic mapping. The muscovite spectrum displays a 2.20 μm absorption feature; whereas kaolinite and alunite exhibit 2.17 and 2.20 μm absorption features. The numbers across the top of the graph indicate the ASTER band center positions (Clark et. al., 1993b).

5.3.1.2 Phyllic Band Ratio

A spectral analysis of ASTER image spectra and resampled ASTER laboratory spectra showed that band ratio 4/6, 5/6, and 7/6 were needed to map the 2.17 and 2.22 absorption features there by delineating argillic and phyllic altered rock (Figs. 18B &

19). Band ratios 4/5 and 4/6 map the 2.165 and 2.2 absorption features, respectively.

ASTER spectra of phyllic altered rocks show band 5 is at least 5% greater than band 6, which indicate all 5/6 band ratio values greater than 1.05 classified as phyllic-altered rock ASTER spectra also indicate that band 6 is at least 25% lower than band 4, and band 7 is at least 3 % greater than band 6. Value in the band ratio algorithm for band ratio 4/6 and 7/6 must be greater than 1.25 and greater or equal to 1.03, respectively in order to classify pixel as phyllic alteration (Figs. 18B & 19).

5.3.1.3 Iron oxide/hydroxide Band Ratio

Iron oxide minerals are developed around many mineral deposits due to oxidation of sulfide minerals. Hematite, Goethite, Jarosite are diagnostic iron oxide minerals associated with hydrothermal process.

For this study ratio image of ASTER band 2 / band 1 is used and pixel value in the band ratio greater than 1.4 classify as iron oxide/hydroxide alteration. Iron oxide threshold value is taken from mean plus two standard deviation statistics of the ratio image.

5.3.1.4 Band Ratio Hydrothermal Alteration Map

Argillic alteration mapped by band ratio mainly occurs in the southwestern and northeastern part of the study area and mapped across different geological units (Fig. 20 & 23). Phyllic-altered rocks in study area are insignificant.

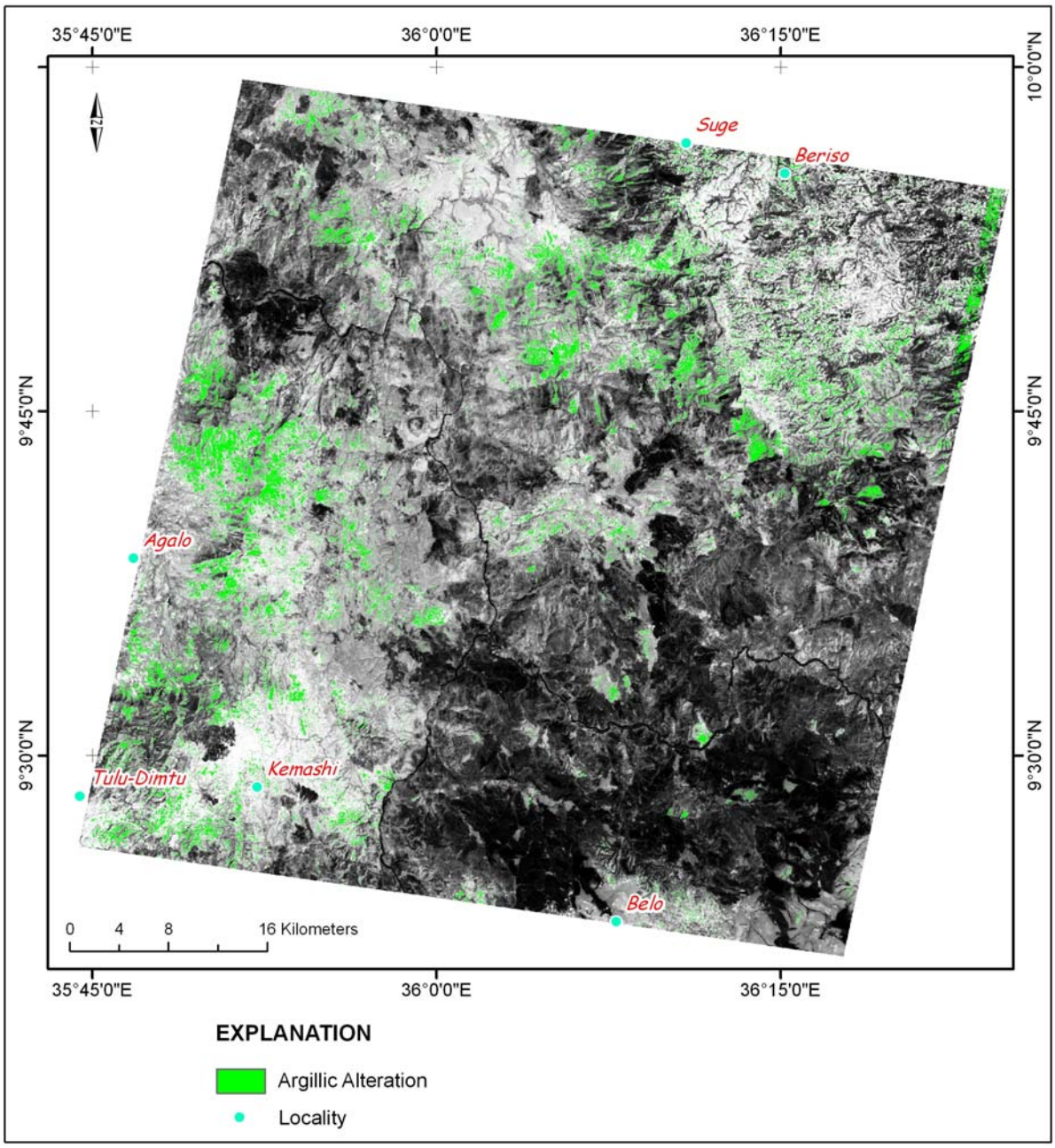

Figure 20. Map of Argillic alteration superimposed on ASTER band 4 image.

The iron oxide/hydroxide alteration mainly mapped in the northeast part of the study area and bounded in the Tertiary volcanic and Paleozoic sedimentary units (Fig. 21 & 22). The Tertiary basalt at this part of the area has a uniquely narrow width about an average of 4 km and stretched north-south about 30 km and it extends to the north out of the study area.

In the field the Tertiary basalt appears black when it is fresh and yellowish brown when it is weathered. The unit is formed of aphanitic and amaygdaloidal intercalation. Thin section study by Solomon, et al., 2000 indicates the rock is composed of plagioclase (35%), Olivine (35%), augite (25%) and opaque minerals (5%).

The Paleozoic sediment (sandstone) unit at this part of the study area also shows strong iron oxide alteration. From field observation the unit appears yellow, fine grained and constitutes quartz, white mica and some opaque minerals. Thin section study by Solomon, et al., 2000 indicate the unite composed of 50% rock fragments, 40% quartz, 7% silica cement, 2% hematite and trace amount of opaque minerals and amphibole.

Both units mapped at other part of the study area didn't show iron oxide/hydroxide alteration and the present work field observation and thin section studies by the previous workers couldn't explain the high iron oxide alteration at this part of the study area. But the alteration patterns suggest the abundance is correlated with the lithologic units.

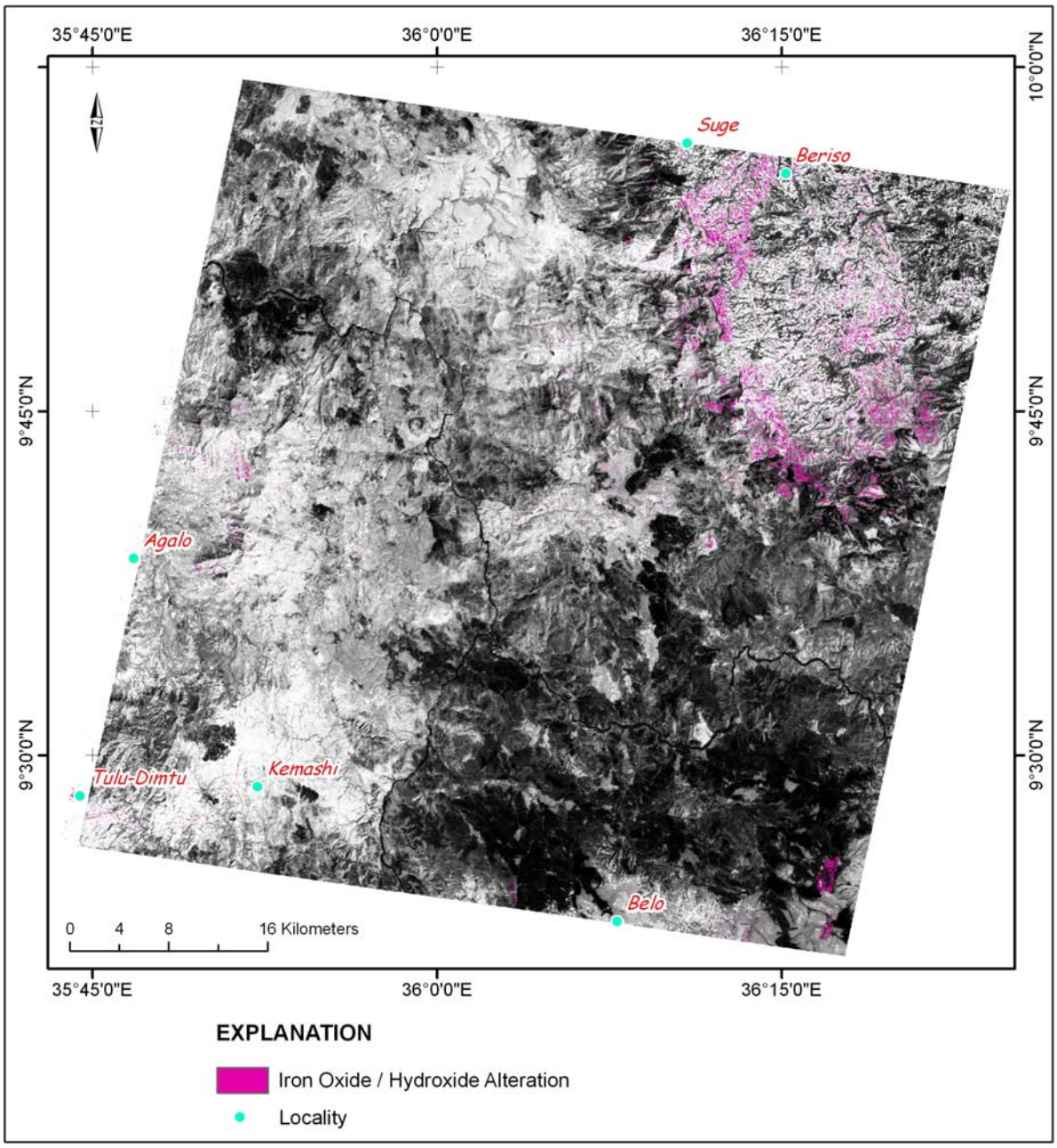

Figure 21. Map of iron oxide/hydroxide alteration superimposed on ASTER band 4 image.

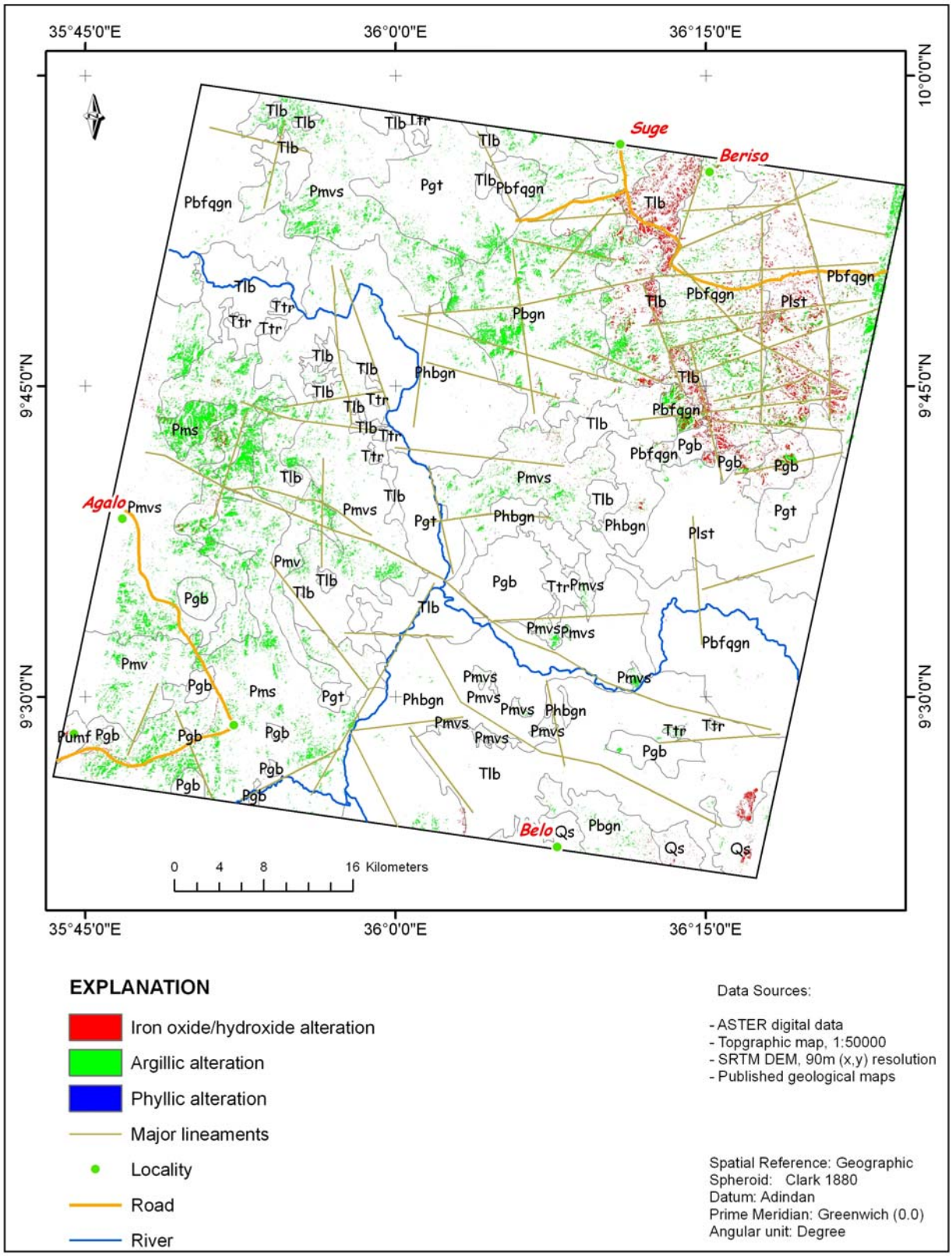

Figure 22. Argillic, Phyllic & Iron oxide/hydroxide alteration draped over geological interpreted map of the study area.

5.3.2 Alteration Mapping Using Feature Oriented Principal Component Analysis (FPCA)

Background

PCA is a powerful statistical technique that can use for suppressing irradiance effects that dominate all bands, therefore enhancing spectral reflectance features of geological material (Crosta et al., 2003). Crosta and Moore (1989) developed a technique based on PCA for mapping iron oxide/hydroxides using Landsat TM. The technique called "feature oriented principal component selection (FPCS)". The technique establishes the relationship between the spectral responses of target materials and numeric values extracted from the eigenvector matrix used to calculate the principal component (PC) images. Using this relationship, they were able to determine which PC images contained the spectral information of an intended target.

This technique modified by Loughlin (1991), by applying PCA transformation on specific Landsat TM bands, this done to avoid other material would not be mapped and the spectral information due to target materials to be mapped into a single PC image. The procedure proposed by Loughlin used selected Landsat TM bands for driving spectral information related to iron oxide/hydroxide and hydroxyl-bearing minerals uniquely mapped into PC3 and PC4.

The modified "Crosta technique" has been used for mineral exploration purpose by various workers (ex, Tangestani and Moore, 2001, Souza Filho and Drury, 1998). The idea of applying PCA to drive mineral abundance map using high spectral resolution data comparable to ASTER were proposed by Crosta et al., (1996) and Prado and Crosta (1997).

For this study key alteration mineral mapping was conducted using PCA of ASTER data covering the study area by adapting Crosta technique provided by Loughlin (1991). The key alteration minerals mapped in the study area are alunite, illite and

kaolinite, which are typical mineral end member of argillic and advanced argillic hydrothermal alteration.

Subsets of ASTER bands for FPCA application were selected according to the position of characteristic spectral features of the minerals in the VNIR and SWIR portion of the spectrum (Fig. 23). The subsets of selected ASTER bands for each selected key alteration minerals are shown on Table 9.

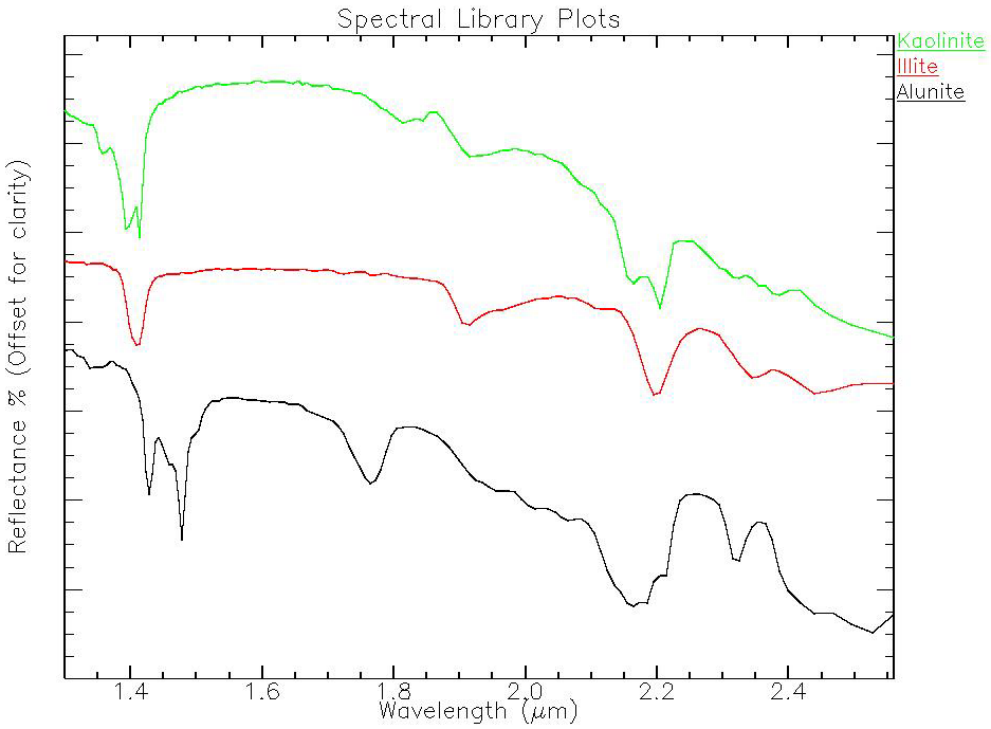

Figure 23. Reference spectra of kaolinite, illite and alunite used for the analysis of characteristic spectral features of the minerals.

Table 9. ASTER bands (VNIR & SWIR) used to map key alteration mineral in the study area using FPCA.

Alteration Minerals			
Kaolinite		Illite	Alunite
ASTER bands	1	1	1
	4	3	3
	6	5	5
	7	6	7

After applying FPCA, the eigenvector matrix used to calculate PCA for each subset was studied to identify which PC contained the target (mineral) information. The PC that contains the target spectral information shows the highest eigenvector loadings from the ASTER bands, coinciding with the target's most diagnostic features, but with opposite signs (+ or -).

5.3.2.1 Kaolinite Mapping

Kaolinite has high reflectance value in ASTER band 4 and 7 and absorbs strongly in band 1 and 6 (Fig 23); the PCA eigenvector statistics of these bands (Table 10) shows that PC2 has high and negative loadings from band 1 (- 0.840) and high and positive loading from band 4 (0.536), indicating that pixels likely to contain kaolinite will be presented by low (dark) Digital Number (DN) values in PC2. Loading for band 6 and 7 shows significantly lower values (-0.030 and -0.081, respectively).

Table 10. Eigenvector statistics for ASTER band 1, 4, 6, and 7 selected for identifying spectral response from kaolinite.

	PC1	PC2	PC3	PC4
Band 1	0.384	-0.840	-0.381	0.047
Band 4	0.687	0.536	-0.473	0.131
Band 6	0.484	-0.030	0.463	-0.742
Band 7	0.383	-0.081	0.646	0.656

The result indicate that the relevant spectral information will be shown by the spectral contrast of kaolinite is the wavelength position equivalent to band 1 and 4. The PC2 image is multiplied by (-1) so that the target material (kaolinite) is displayed as bright pixel (Fig. 24a).

5.3.2.2 Illite Mapping

Illite has high reflectance value in ASTER bands 3 and 6 and absorbs strongly in band 1 and 5 (Fig. 23); the PCA eigenvector statistics of these bands (Table 11) shows that PC3 has high and negative loadings from band 1 (-0.928) and high and positive loading from band 3 (0.300), this indicates that pixels likely to contain Illite will be presented by low (dark) Digital Number (DN) values in PC3.

Table 11. Eigenvector statistics for ASTER band 1, 3, 5, and 6 selected for identifying spectral response from Illite.

	PC1	PC2	PC3	PC4
Band 1	0.321	0.166	-0.928	-0.090
Band 3	0.430	0.852	0.300	0.010
Band 5	0.572	-0.352	0.204	-0.712
Band 6	0.621	-0.351	0.084	0.696

Loadings for band 5 and 6, (-0.030 and -0.081, respectively) are significantly lower value. The result indicates the relevant spectral information will be shown by the spectral contrast of illite in the wavelength position equivalent to band 1 and 3. To display illite as bright pixels in its abundance image (Fig. 24b) all pixel value of PC image were multiplied by (-1).

5.3.2.3 Alunite Mapping

Alunite has high reflectance value in ASTER bands 1 and 7 and absorbs strongly in band 3 and 5 (Fig. 23). The PCA eigenvector statistics of these bands (Table 12) shows that PC3 has high and negative loadings from band 1 (-0.792) and high and positive loading from band 7 (0.476), this indicates that pixels likely to contain alunite will be presented by low (dark) Digital Number (DN) values in PC3.

Table 12. Eigenvector statistics for ASTER band 1, 3, 5, and 7 selected for identifying spectral response from Alunite.

	PC1	PC2	PC3	PC4
Band 1	0.399	-0.460	-0.792	0.041
Band 3	0.747	0.662	-0.006	0.056
Band 5	0.396	-0.380	0.382	-0.744
Band 7	0.355	-0.453	0.476	0.665

Loadings for band 3 and 5 (-0.006 and 0.382, respectively) are significantly lower value. The result indicates that the relevant spectral information will be shown by the spectral contrast of alunite in the wavelength position equivalent to band 1 and 7. The PC3 image was negated so that the target mineral (alunite) is displayed as bright pixels (Fig. 24c).

5.3.2.4 Key Alteration Minerals Color Composite Map

RGB colure composite image for Kaolinite, Illite and Alunite (PC2, PC3 and PC3) is presented in Figure 25.

The possible development of high clay alteration (Kaolinite, Illite and Alunite) in the study area are represented by bleached (whitish) color in the composite image and make major linear zone at the south west part of the study area. An Illite alteration represented by green color in the composite image is the next second dominant alteration in the study area

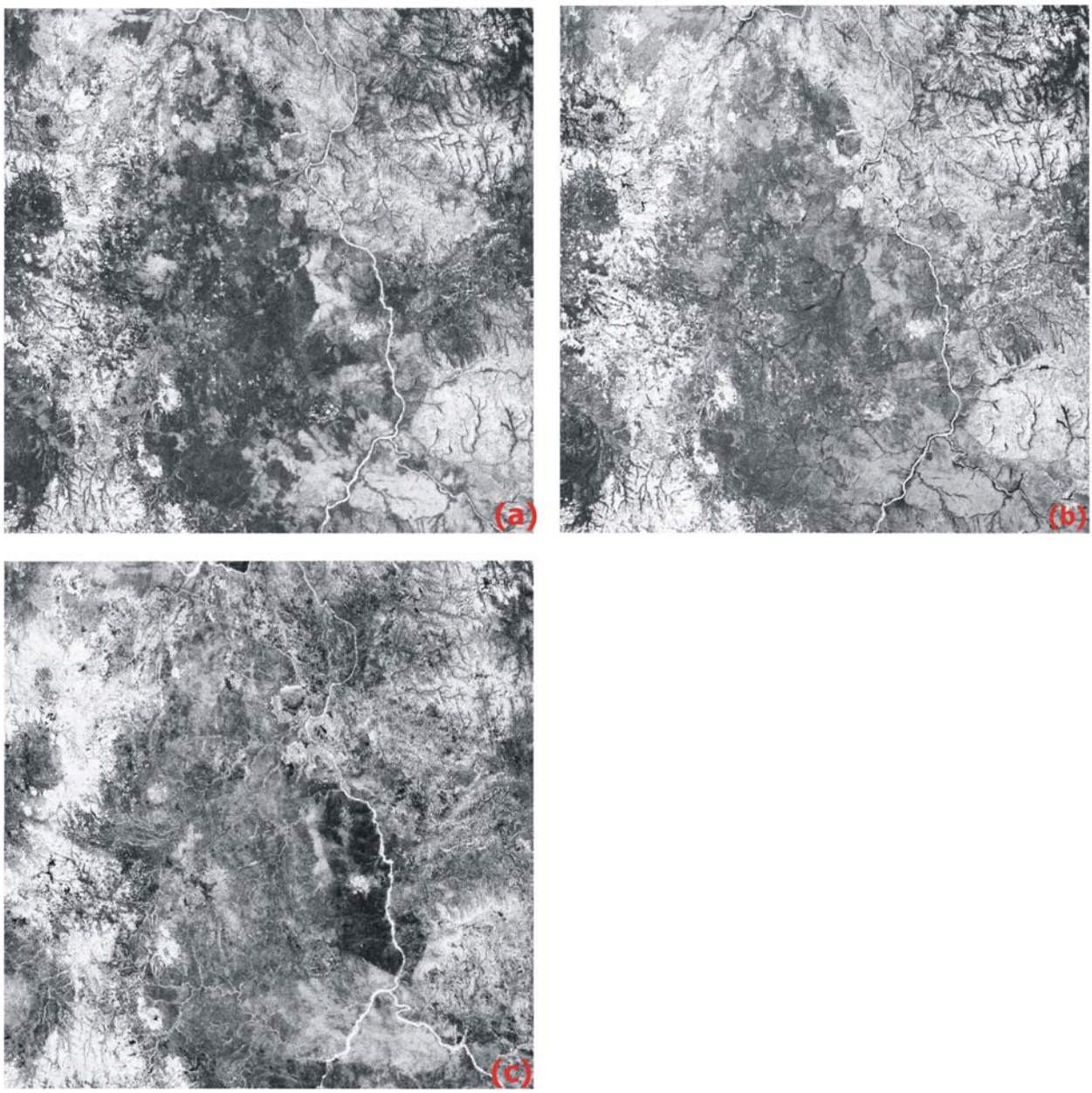

Figure 24. Mineral abundance image of a) kaolinite b) illite c) alunite.
Bright DN values indicate high abundance. The images are subset of the study area approximately 30 km across.

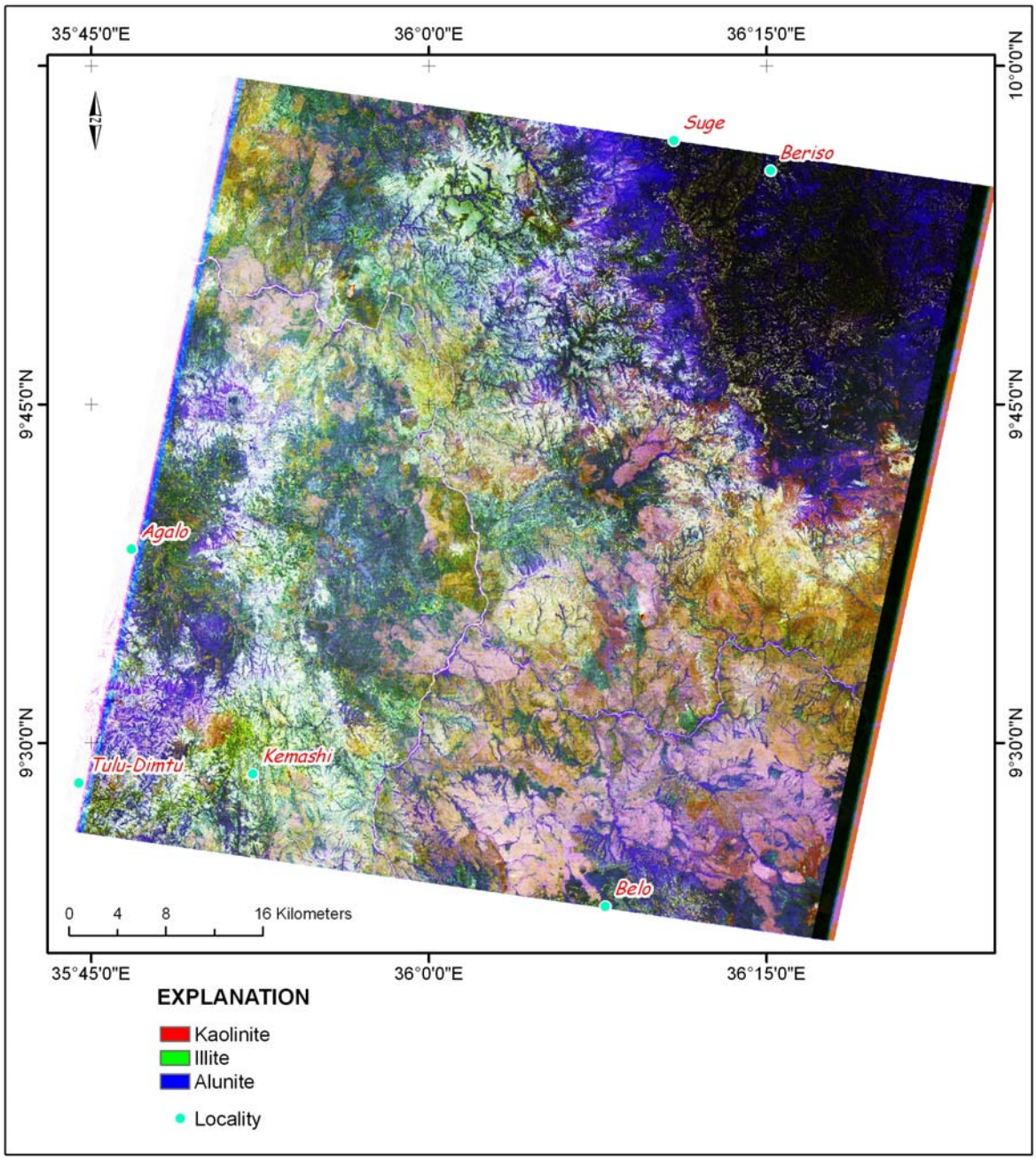

Figure 25. PC color composite image of Kaolinite (PC2), Illite (PC3), and Alunite (PC3) minerals in R, G, and B respectively.

A close study of the PC color composite image of the key alteration minerals (Fig. 25) reveal most interesting results that is presented with respect to specific locations (Fig. 26).

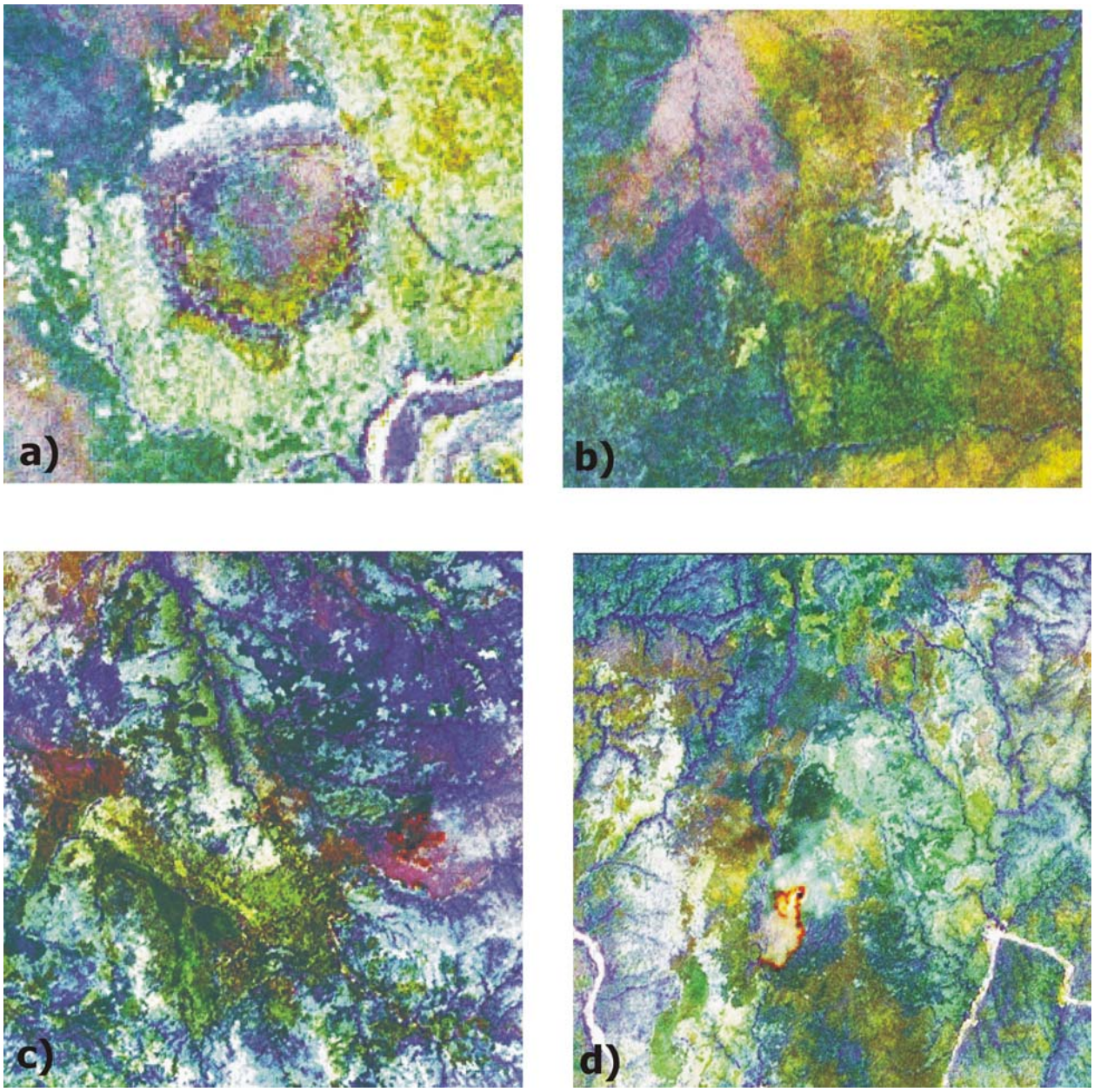

Figure 26. A closer look of PC color composite image of key alteration minerals.
(a) at 35.99E & 9.74N, well developed concentric alteration zone, white (bleached) tone represent high clay alteration (kaolinite, illite & Alunite); green tone - illite dominant; blue tone - alunite abundance; violate tone (rime of the ring) - abundance of kaolinite. (b) At 35.99E & 9.74N, white (bleached) tone high clay alteration (kaolinite, illite & Alunite) located at the top of ridge enclosed by green tone - illite dominant alteration zone. (c) At 35.092E &

9.88N, green tone - illite dominant alteration developed along major fractures; red tone - kaolinite dominant alteration. (d) At 35.94E & 9.84N, elliptical shaped alteration zone developed at the inner part of fold hinge structure. The center of the alteration zone white (bleached) high clay alteration followed by pink to red tone kaolinite alteration zone and blue tone alunite alteration and the outer part is dominated by green tone illite alteration.

5.3.2.5 Key Alteration Minerals Abundance Map

To distinctively map the alteration minerals shown in Table 9, mineral abundance image were produced from ASTER data using FPCA technique. In which bright DN values indicate high mineral abundances (Fig. 24).

In order to show high abundance alteration by separating the background and to represent in different color, the DN values of the PC images of the alteration minerals constrained using images statistics. DN Value greater than mean plus two standards deviation were taken as possible spread abundance for each alteration minerals. Kaolinite, Illite and Alunite mineral abundance map displayed as red, green and blue layers respectively (Fig. 27 & 28).

In this image, kaolinite alteration (Red) is insignificant and is found mainly associated with the syn-post tectonic granite and gabbroic units at the central east and central part of the study area. Illite as green color is mapped at the southwestern part of the area. Alunite is mapped at the southwest and central north part of the study area.

Yellow color indicates a mixture of illite and kaolinite. This result is in agreement with alteration mapping resulted from band ratio technique.

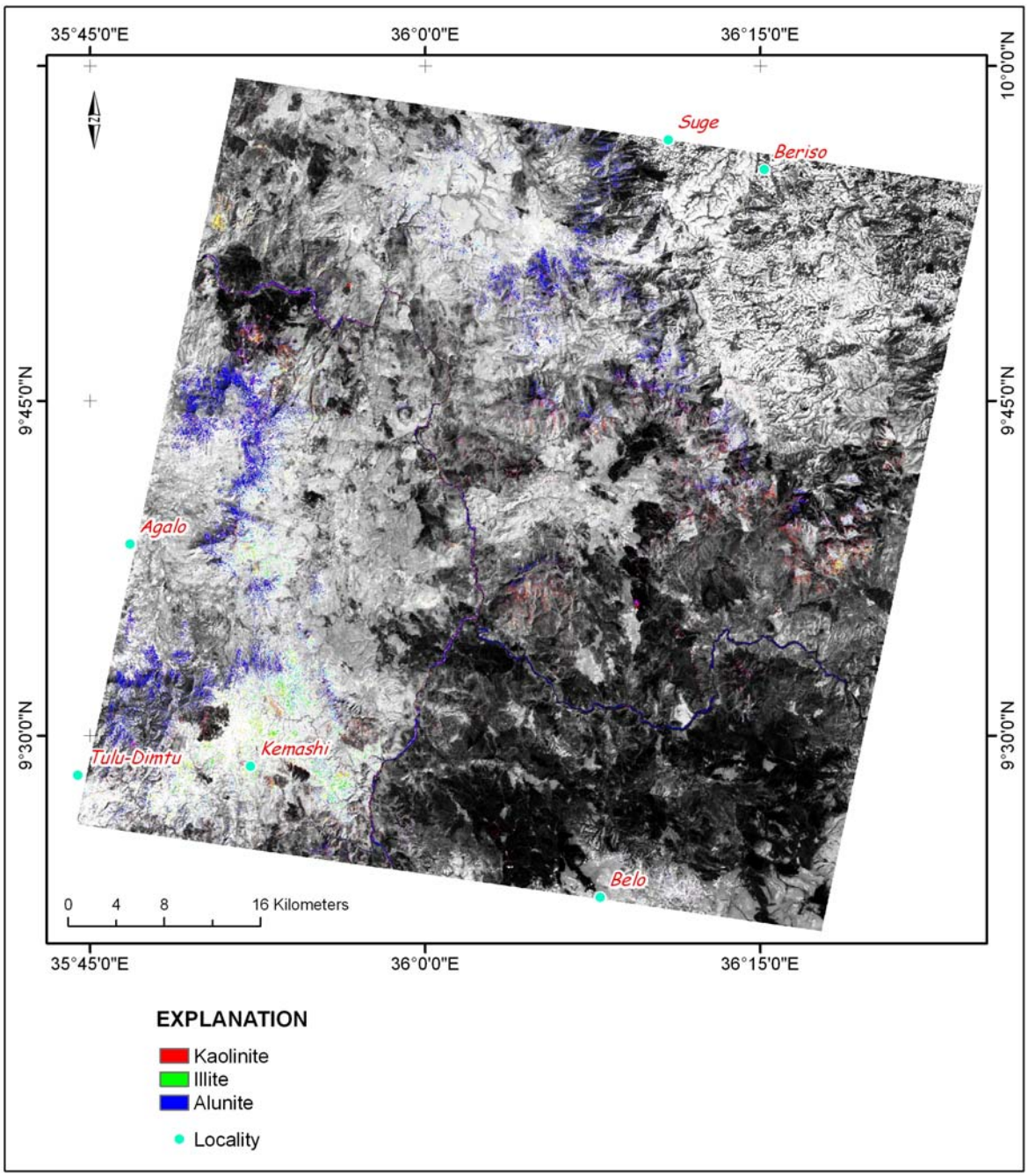

Figure 27. Kaolinite, Illite and Alunite abundance color composite in RGB images draped over ASTER band 4.

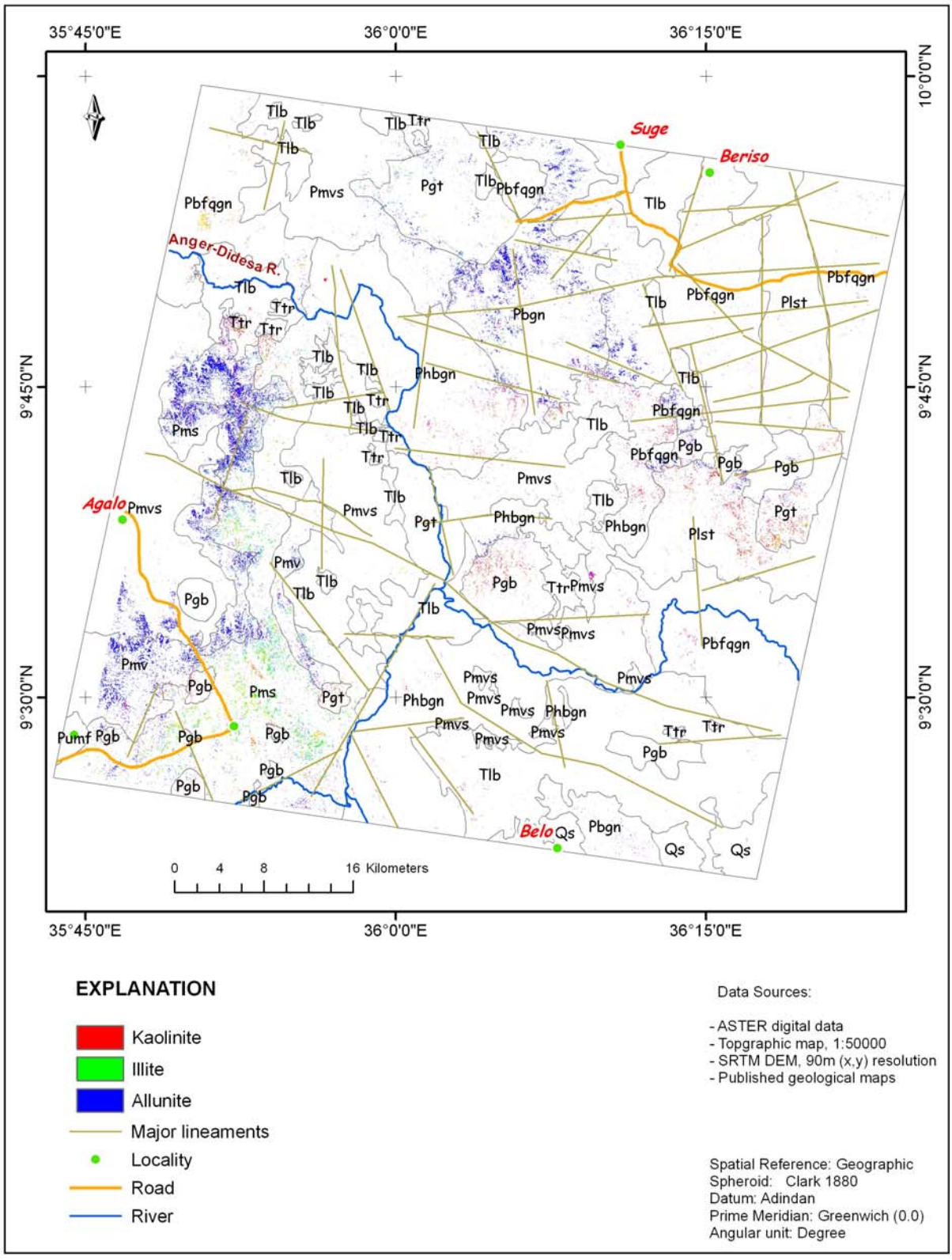

Figure 28. Kaolinite, Illite and Alunite abundance image draped over geological interpreted map of the study area.

ASTER mapped Kaolinite, Illite and Alunite alteration (Fig. 27) extends across different geological units includes the recent volcanics and crystalline basement rocks and also related to different structures in the study area. The following figures (Fig. 29 A, B & C) show some examples of alterations mapped at southwest and northwest quadrants of the study area.

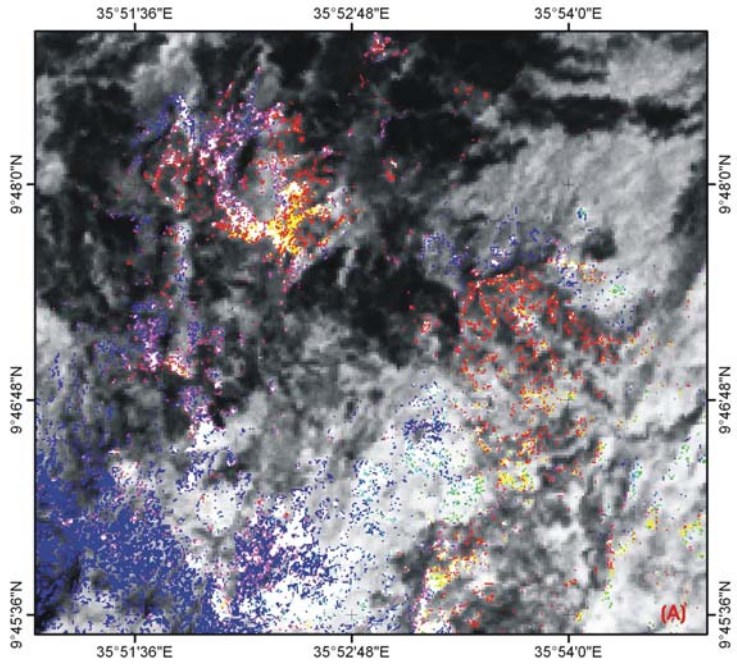

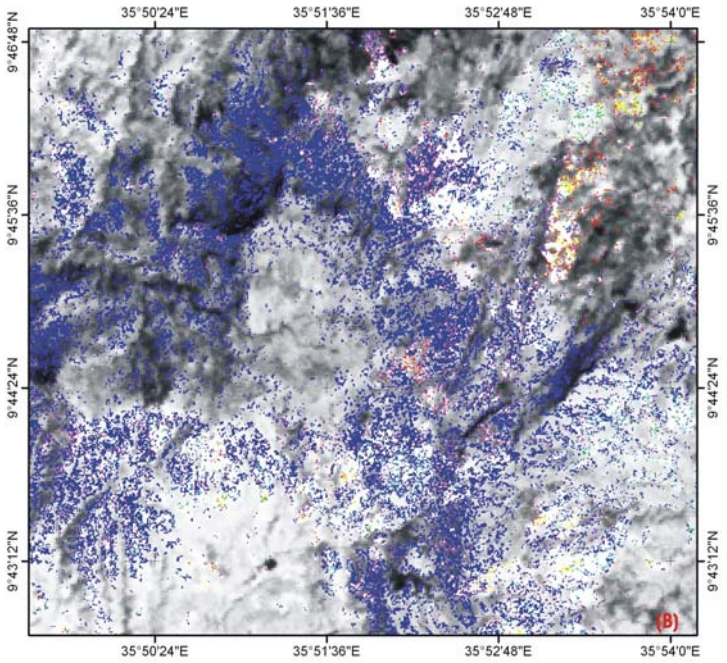

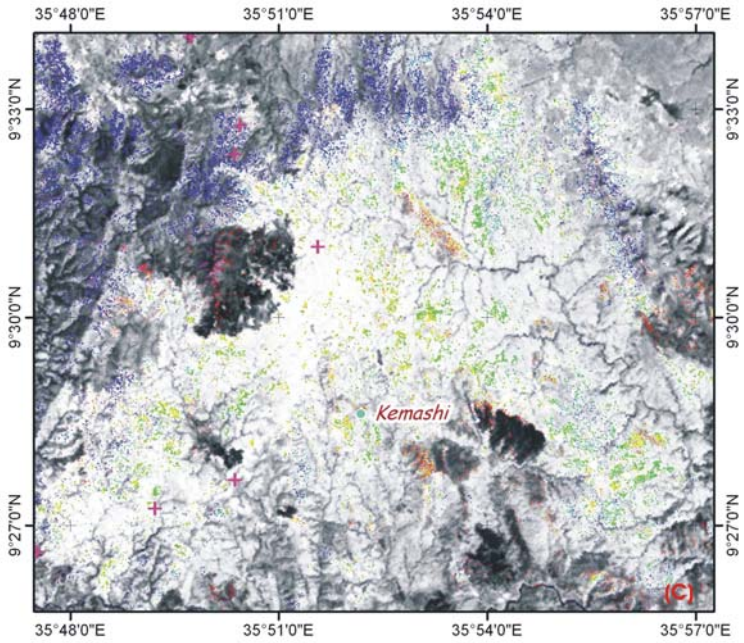

Figure 29. Map showing Kaolinite, Illite and Alunite alteration in different geological environments in the study area.
(A). Alteration related to recent volcanics. At the northern part of the figure circular alteration pattern around the rim of Trachyte plug is shown.
(B) Alteration related to fold structure. In the north western part of the study area the Alunite alteration forms linear patterns associated with fractures trend in the NE, NW and EW direction. (C). Lineament related alteration. In the vicinity of Kemashi town, Illite and Alunite follow foliation and lineament in the volcano sedimentary basement rocks. Kaolinite (Red), Illite (Green) and Alunite (Blue).

5.4 Field Study

One field visit with a total of 10 days was conducted during May 14 – 23, 2009 for verification of the preliminary interpretation results. Due to inaccessibility of the study area, only the southwest and northeast parts were visited.

Global positioning system (GPS), topographic maps (1:50000 scale) and interpreted maps resulted from this study were used. Spatial position of field observation points and note on observations were recorded and summarized in Table 13 and shown on Figure. In the southwestern part of the study area, northwest of Kemashi town, two main observations were made.

1) On the published geological map at this locality the gabbroic unite mapped as one narrow elongated body but the interpreted results and field observation shows the units are not single body and they preserve their elliptical intrusive morphology. 2) Most of the rocks around Kemashi town show strong chlorite, sericite and epidotes alteration and this confirm the interpreted result successful alteration mapping.

In the northeast part of the study area the interpreted result mapped three lithologic units using slight spectral difference between the units under vegetation cover. The field visit also verifies the presence of the lithologic units as interpreted and this proves the effectiveness of ASTER data and different image enhancement methods for lithologic mapping under tolerable vegetation cover. In this part of the area where the processed image result high iron oxide/hydroxide alteration were also visited and confirm that the two iron oxide altered rocks are the Tertiary basalt and Paleozoic sediment (sandstone).

Table 13. Field visit observation summery.

Sample No.	Longitude	Latitude	Rock type	Alteration
AU_001	35.77504	9.64978	Serpentine	Serpentinization
AU_002	35.77994	9.65008	Graphitic Quartzite	Oxidized
No sample	35.78300	9.65105	Graphitic Quartzite	Oxidized
AU_003	35.78656	9.65047	Diorite	
AU_004	35.79829	9.63760	Biotite Granite	
AU_005	35.80136	9.98736	Amphibolites	
AU_006	35.81361	9.57136	Basic Intrusive	Oxidized
AU_007	35.82130	9.57069	Silicious rock	epidotized
AU_008	35.82892	9.56751	Gabbro	Oxidized
AU_009	35.84087	9.54625	Metavolcanics	Clay, sericite, chlorite
AU_010	35.83957	9.53916	Basic Intrusive	Chlorite, sericite
AU_011	35.85953	9.51699	Biotite Granite	
AU_012	35.83964	9.46091	Metasediment	Silicification, sericite
AU_013	35.82045	9.45402	Gabbro	
AU_014	35.79210	9.44368	Chlorite schist	Chlorite, sericite
No sample	36.17702	9.95587	Biotite Granite	Oxidized
No sample	36.17702	9.93459	Biotite-feldspar-quartz gneiss	Oxidized
AU_015	36.17968	9.92320	Granite	
No sample	36.18336	9.91840	Biotite-feldspar-quartz gneiss	
AU_016	36.18322	9.90605	Basalt	
AU_017	36.22806	9.89425	Basalt	
No sample	36.26380	9.92151	Biotite-feldspar-quartz gneiss	
AU_018	36.28005	9.91954	Biotite-feldspar-quartz gneiss	
AU_019	36.31604	9.89607	Sandston	

6 DISCUSSION

In this study, different digital image processing techniques were applied to ASTER reflectance data (VNIR & SWIR) aimed at lithological, structural and hydrothermal alteration mapping in the study area.

False color composite of raw ASTER bands and PC transformation provides best images with overall good lithological information. Contrast stretching of input data further enhances the spectral contrast between different lithologic units and greatly facilitates the visual lithologic interpretation. Thin section mineralogical composition of different lithological units obtained from the published geological maps and reports also utilized to understand the spectral properties of the different lithologies.

Lithologic interpretation at some places of the processed images was difficult because of the complexity of the geology and due to little contrast in mineralogy of certain lithologic units. The typical examples include the Paleozoic sediments and the Biotite-feldspar-quartz gneiss at the eastern part of the area both appear pink colored. The Tertiary basalt and the hornblende-biotite gneiss units appear blue in the PC color composite image but well discriminated in the enhanced false color composite image of raw ASTER data.

Vegetation covers at the northeast part of the study area masked spectra of rocks in the processed images and make lithologic interpretation difficult. However, slight color variation and textural (morphological) difference and filed visit helps for lithologic discrimination in this part of the area

Lithological name for the interpreted geological map were used mainly based on the published geological maps but one lithological name were modified based on field observation by this study. Accordingly the Quartzo-feldspathic gneiss mapped in the northeast part of the study area by the previous work were renamed as Biotite-feldspar-quartz gneiss because the present field study shows the unite contains considerable amount of biotite in addition to feldspar and quartz.

In the Nekemt sheet geological map published by GSE the "undifferentiated gneiss" unites reported as a mix of various gneisses including hornblende-biotite gneiss but the same unite western extension mapped in Gimbi sheet geological map by GSE named as hornblende-biotite gneiss. For this study, the hornblende-biotite gneiss is taken as the unit name for the interpreted geological map.

The quartz-mozonit-monzodiorite unit mapped in the southwest part of the study area by the published geological map were omitted and mapped as metavolcano-sedimentary unit in the ASTER interpreted map. Because the present field work mapping in this particular area shows the presence of mix of various rock units including quartz diorite, graphitic quartzite, amphibolites and patches of meta-granite. And it is mapped as metavolcano-sedimentary unit because of its spectral similarity of the unit in other part of the processed images.

In order to asses the quality of the interpreted geological map resulted from ASTER data, comparison were made with the previous geological maps done by conventional ground mapping method. Visual inspection was made by overlapping the interpreted geological map and the existing compiled geological map in a GIS, using vector and thematic layers.

The comparison was made mainly based on the shape, pattern, size, geological structures, morphological information and spatial relationships between different litho-stratigraphic units in the study area. For systematic approach and simplification of comparison the study area were split in to four equal quadrants.

Northwest quadrant: three major litho units, namely meta-granite, metavolcano-sedimentary rocks and Tertiary basalt were mapped by both methods. The Tertiary basalt in the previous work mapped as north-south stretched single body and at some places it includes the penetrative foliation and other structures, which are clearly observed in the processed ASTER image and hill-shade map of the area. Where as, the interpretation identify the Tertiary basalt by their unique dark tone spectral property and by their semi-circular shape and smooth morphology and

mapped as separate small patches. The meta-granite in the published maps stretched in northwest direction but in the interpreted geological map preserve their semi-circular intrusive morphology. The size, shape, orientation and spatial position of the hornblende-biotite gneiss unit are comparable in both maps.

Northeast quadrant: Biotite gneiss, Biotite-feldspar-quartz gneiss, Paleozoic sedimentary rock and Tertiary basalt are the major litho units and in many respect both the published geological maps and ASTER data interpretation give comparable result. The area in this quadrant covered by vegetation but the processed ASTER image interpretation give good result, which shows the effectiveness of ASTER data for geological mapping even when bed rock are not directly exposed. Drainage and vegetation pattern and subtle spectral difference resulted from the underlying lithology used as main interpretation key.

Southeastern quadrant: meta-granite, meta-gabbro, Paleozoic sedimentary rock and Tertiary basalt are the major units mapped both in the published geological maps and ASTER data interpretation. In the north western part of the quadrant the published geological maps represent the Tertiary basalt as north-south stretched single big unit. But the interpretation result reveals that Tertiary basalt mapped by the previous work encloses folded and spectrally different litho unit. The meta-gabbroic and meta-granite bodies are comparable except some discrepancy in their size and outline shape.

Southwest quadrant: meta-volcano-sediment, meta-gabbroic, meta-ultramafics are the major litho units mapped by both methods. In the published map the meta-gabbroic unit at the southwest corner of the quadrant mapped as single body but the ASTER data interpretation and field verification shows that the unit crop out at three different locations oriented north southerly and appear as semi-circular bodies. The Tertiary basalt in the north eastern of the quadrant covers large area in the published geological map; it is the extension of the same unit from the northwest quadrant. In the ASTER data this unit is mapped as metavolcano-sediments because in the processed ASTER image and hill-shade map the unit exhibited penetrative

foliation and possibly shear related drag folds, which are supposed to be basement structures, and the body spectral property is quit different than the Tertiary basalt unites interpreted in the study area.

Lineaments interpreted from ASTER image and DEM data were also compared with the published geological map structural information. The published map recognizes 96 lineaments and their length range between 0.5 - 13 kilometers. The interpretation map shows about 1105 lineaments. The smallest lineament size is 1 kilometer and the largest is about 40 kilometer. The interpreted lineament map provides all the small and large lineament population in the study area. The smaller lineaments indicate the form and position of the individual folds, joints, lithological contacts. The larger lineaments indicate the general geometry of folds, faults and other structures and provide information on regional structural patterns.

Spatial enhancement of ASTER data and topographic information from SRTM DEM data were found superior methods for lineament mapping in this study. A 3x3 and 7x7 window size high frequency edge detection filters greatly helped to extract surface structures from ASTER data. Hill-shading of SRTM DEM data provides valuable geomorphologic information for the interpretation of regional structure. Foliation, folds and fracture system of various orientations are major structural elements recognized from the processed images. The result of interpreted structural information is in agreement with the different deformation events mapped on the published geological maps of the area. But the interpreted results greatly enhance the structural data of the area by supplementing detail structural information.

In order to produce alteration mineral abundance image for some alteration minerals "Feature Oriented Principal Component Analysis (FPCA)" and "band rationing and threshold" image processing techniques were applied using ASTER reflectance datasets. VNIR-SWIR wavelength region of ASTER data that shows subtle spectral reflectance difference were used as a basis for mapping the surface distribution of alteration minerals, and hence to delineate hydrothermal alteration zone. Hydrothermally altered rocks are distinctive in ASTER image mainly because of

absorption features in 2.17 and 2.2 m due to the presence of OH minerals. Most of hydrothermal alteration in the study area consists of argillic-altered rocks, iron oxide/hydroxide altered rocks and minor amount of phyllic-altered rocks and mapped across various lithologic units.

Because there is no reported mineral occurrence in the study area it is difficult in this study to explain the relationship between mineralization and the obtained geological information.

In general, a comparison of ASTER data interpreted geological map against the published geological maps of the area shows that the ASTER data can be used to add information on the existing geological maps by using various spectral mapping techniques.

7 CONCLUSION

Using remote sensing data combined with DEM is an effective tool for lithologic and geological structure mapping as well as delineating mineral alteration zone.

Analyzing of remote sensing and DEM data covering the study area have shown.

1. The effectiveness of applying ASTER reflectance data for geological mapping, through the identification and interpretation of subtle spectral difference between different rock units.

2. The study illustrates the effectiveness of ASTER remote sensing data and edge-enhancement techniques for lineament mapping and the applicability of SRTM DEM for mapping geological structures on the basis of their geomorphologic expression.

3. The usefulness of ASTER reflectance data and the two robust image processing methods (Band rationing and feature oriented principal component transformation) to delineate hydrothermal alteration zone.

4. The overall result of this study demonstrates that remote sensing method using multi-spectral data can be very useful for regional hydrothermal alteration, structure, lithologic mapping to provide important data for regional mineral assessment and to define target for mineral exploration, particularly in the area of good rock exposure (very minor soil development and small or absence of vegetation) and if the interpretation supported by published geological map and/or sufficient ground truth.

REFERENCES

Abrams, M. J., Hook, S. J. and Ramachandra, B. (2002). *ASTER User Handbook version 2*. Jet Propulsion Laboratory, NASA, 135PP.

Abrams, M. J., Rothery, D. A., and Pontual, A. (1988). *Mapping in the Oman ophiolite using enhanced Landsat Thematic Mapper image*. Techtonophysics, 151, 387-401.

Amenti, A., (1989). *Tectonic history of the Pan-African low grade belt of western Ethiopia*. Ethiopian Institute of Geological Surveys, Note no.305, 14p.

Ayalew, T., Bill, K., Moore, J.M., and Paris, R.R. (1990). *U-Pb and Rb-Sr geochronology of the western Ethiopia Shield*. Geological Society of America, Bulletin 102, 1309-1316.

Berhe, S. M., (1990). *Ophiolites in northeast and east Africa: Implementation for Protrozoic crustal growth*. Journal Geological Society of London 147, 41-57.

Chavez, P. S., Berlin, G.L., and Sowers, L.B. (1982). *Statistical method for selecting Landsat MSS ratios*. Journal of Applied Photograph Eng., 8, 23-30.

Clark, R. N., King, T.V.V., Klejwa, M., Swayze, G. and Vergo, N. (1990). *High Spectral Resolution Reflectance Spectroscopy of Minerals*. Journal of Geophysical Research, 95, 12653-12680.

Clark, R. N., Swazye, G. A., Gallagher, A., King, T. V. V., and Calvin, W.M., (1993b), the U.S. Geological Survey. *Digital Spectral Library*: Version 1:0.2 to 3.0 microns: http://speclab.cr.usgs.gov

Crane, R. B (1971). *Processing techniques to reduce atmospheric and sensor variability in multispecteral scanner data*. Proceeding 7th International symposium Remote Sensing and Environment, 2, 1345-1355.

Crosta, A. P., and Moor, J. Mc M., (1989). *Enhancement of Landsat Thematic Mapper imagery for residual soil mapping in SW Minas Gerais State Brazil: a prospecting case history in greenstone belt terrain*. Proceeding of the 9th Thematic Conference on Remote Sensing for Exploration Geology, Calgary (Ann Arbor, MI: Environmental Research Institute of Michigan), pp, 1173-1187.

Crosta, A. P., Prado, I.D.M., and Obara, M., (1996). *The use of Geoscan AMSS Mk-II data for gold exploration in the Rio Itapicuru greenstone belt, Bahia, Brazil.* Proceeding of the 11th Thematic Conference on Remote Sensing for Exploration Geology, LasVegas, NV (An Arbor, MI: Environmental Research Institute of Michigan), pp. 205-214.

Drury, S., (1986). *Remote sensing of geological structure in temperate agricultural areas*. Geological Magazine, 123, 113-121.

ERDAS (ed.) (1982-1994). *Erdas Field Guide*. Atlanta (ERDAS, Inc.)

Ethiopian Mapping Agency, (1981). *National Atlas of Ethiopia, preliminary edition*. Ethiopian Government, Addis Ababa

Getanneh, A. (1991). *Lithostratigraphy and environment of deposition of Late Jurassic-Early Cretaceous sequence of central part o north western platu, Ethiopia*. N. Jb. Geol.Palantology, Abh., vol.180, 255-284.????

Gillespie, A. R., Kahle, A. B. and Walker, R. E. (1986). *Color enhancement of highly correlated images, decorrelation and IHS contrast stretches*. Remote Sensing Environment, 2, 209-235.

Greenwood, W. R., Hadely, D. G., Anderson, R. W., Fleek, R. and Schmidt, D. L., (1976). *Late Protrozoic cratonization in southwestern Saudi Arabia. Royal Society of London, PhD*. Trans. Ser. A. 280, 517-527.

Guilbert, J. M. and Park, C. F. Jr. (1986). *The Geology of Ore Deposits*, 985pp.

Hunt, G. R., and Salisbury, J. W., (1970). *Visible and near infrared spectra of minerals and rocks – 1. Silicate minerals*. Modern Geology, v.1, no.4, 283-300.

Hunt, G. R. and Salisbury, J.W. (1971). *Visible and near infrared spectra of minerals and rocks: II carbonates*. Modern Geology, 2, 23-30.

Hunt, G. R. (1977). *Spectral signatures of particulate minerals, in the visible and near infrared*. Geophysics, 42, 501-513.

Hunt, G. R. and Salisbury, J.W. (1977b). *Visible and near infrared spectra of minerals and rocks: I silicate minerals*. Modern Geology, 2, 195-205.

Hunt, G. R. and Ashley, R.P. (1979). *Spectra of altered rocks in the visible and near infrared*. Economic Geology, 74. 1613-1629.

Hunt, G. R. and Ashley, R.P. (1997??). *Spectra of altered rocks in visible and near infrared*. Economic Geology, 74, 1613-1629.

Jensen, J. R., (1996). *Introductory Digital Image Processing*. Prentice Hall Series in Geographic Information Science, New Jersey, 316p.

Kazmin, V. (1979). *Stratigraphy and correlation of volcanic rocks in Ethiopia*. Geological Survey of Ethiopia Internal Report.

Kenea, N. H. (1979). *Digital Enhancement of Landsat Data, Spectral Analysis and GIS Data Integration for Geological Studies of the Derudeb Area, Southern Red Sea Hill, NE Sudan. (Doctoral Thesis).* Berlin, Geowiss. Abh., D, 14, 116pp.

Lillesand, T.M., Kiefer, R.W. and Chipman, J.W. (2004). *Remote Sensing and Image Interpretation.* 5th ed., 763pp.

List, F. K. (1993). *Fundamentals of digital image processing for geological application*. Proceeding of the 4th United Nations Ins. Training Course on Remote Sensing Application to Geological Science. Berliner Geowiss Abh. D, 5, 7-29.

Liu, C. C., Sousa Jr., M. A. and Gopinath, T.R. (2000). *Regional structural analysis by remote sensing for mineral exploration, Paraiba state, Northern Brazil*. Geocarto International, 15, 69-75.

Loughlin, W., (1991). *Principal Component Analysis for alteration mapping*. Photogrammetric Engineering and Remote Sensing, 57, 1163-1169.
Lowell, J. D., and Guilbert, J.M., (1970). *Lateral and vertical alteration mineralization zoning in porphyry ore deposits*. Economic Geology and the Bulletin of Society of Economic Geologist, v.65, no.4, p. 373-408.

Mars, J. C. and Rowan, L. C. (2006). *Regional mapping of phyllic and argillic altered rocks in the Zagros magematic arc, Iran, using Advanced Space born Thermal Emission and Reflection Radiometer (ASTER) data and logical operator algorithms*. Geospher, v.2; no. 3; p. 161-186.

Mengesha, T., Tadiwos, C. and Workneh, H. (1996). *Explanation of the Geological Map of Ethiopia*.

Meyer, C. and Hemley, J.J. (1967). *Wall rock alteration. Geochemistry of Hydrothermal Ore Deposits* (ed. H.L. Barnes), pp. 166-235.

More, P., (1971). *Outline Tectonics of Ethiopia*. Tectonic of Africa (Earth Sciences, 6) UNESCO. 1971.

O'Leary, D. W., Friedman, J.D. and Pohn, H. A. (1976). *Lineament, linear and lineation. Some proposed new standards for old terms*. Geological Society of America Bulletin, 87, 1463-1469.

Prado, I. D. M., and Crosta, A. P., 1997. *Evaluating Geoscan AMSS Mk-II for gold exploration in the Fazenda Maria Preta District, Rio Itapicuru greenstone belt, Bahia State, Brazil*. Bulletin IG-USP, 28, 63-84.

Rajesh, H.M. (2004). *Application of remote sensing and GIS in mineral resource mapping – An overview.* Journal of Mineralogy and Petrological Sciences, Volume 99, page 83-203, 2004.

Rein, B. and Kufmann, H. (2003). *Exploration for gold using panchromatic stereoscopic intelligence satellite photographs and Landsat TM data in the Hebi area, china*. International Journal of Remote Sensing, 24, 2427-2438.

Rothery, D. (1987). *Improved discrimination of rock units using Landsat Thematic Mapper imagery of the Oman ophiolite*. Journal of the Geological Society of London, 144, 587-597.

Rothery, D. (1987). *Improved discrimination of rock units using Landsat Thematic Mapper imagery of the Oman ophiolite*. Journal of the Geological Society of London, 144, 587-597.

Rose, A. W. and Burt, D. M. (1979). *Hydrothermal alteration. Geochemistry of Hydrothermal Ore Deposits*, 3rd edn. (ed. H.L. Barnes), pp. 303-365.

Rowan, L. C. and Bowers, T. L. (1995). *Analysis of Linear Features Mapped in Landsat Thematic Mapper and side-Looking Airborne Radar Images of the Reno 1° by 2° Quadrangle, Nevada and California: Implications for Mineral Resource Studies*. Photogrammetric Engineering and Remote Sensing, 61; 749-759.

Rowan, L. C., Wetlaofer, P.H., Gotez, A.F.H., Billingsley, F.C., and Stwart, P.H., (1974). *Discrimination of rock types and detection of hyderothermally altered areas in south-central Nevada*. Geological Survey Professional Paper 883, 35p.

Rowan, L. C., Gotez, A. F. H., and Asheley, R. P., (1977). *Discrimination of hyderothermally altered rocks and unaltered rocks in visible and near infrared multispectral images*. Geophysics, v.42, p. 522-535.

Sabins, F. F. Jr (1987). *Remote Sensing Principles and Interpretation*, 2nd ed., 449 pp.

Schmidt, R. G., (1976). *Exploration for porphyry cooper deposits in Pakistan using digital processing of Landsat-1 image data*. U.S. Geological Survey Journal of Research, v.4, no.1, 27-34.

Siegal B. S., and Gillespie, A. R. (1980). *Remote Sensing in Geology*. New York, Acadamic Press, 702pp.

Solomon, G. and Mulugeta, H. (2000). *Geology of the Nekemet Area*. Memoir 14, Ethiopian Institute of Geological Surveys Internal Report.

Souza Filho, C. R., and Drury, S. A., (1998). *Evaluation of JERS-1 (FUYO-1) OPS and Landsat TM images for mapping of gneissic rock in arid area*. International Journal of Remote Sensing, 19, 3569-3594.

Stern, R. J., (1994). *Arc assembly and continental collision in the Neoprotrozoic East African Orogen: implication for the consolidation of Gondwanaland*. Annual Reviewers of earth and Planetary Science, 22, 319-351.

Tamirat, W. and Timothy R. Astin (19920). The Karoo sediments (Late Paleozoic to Early Jurassic) of the Ogaden Basin, Ethiopia. Sedimentary Geology, 76, 7-21.

Tadesse, A., and Tsegaye, A. (2000). *Geology of the Gimbi Area*. Memoir 15. Geological Surveys of Ethiopia Report.

Tangestani, M. H., and Moore, F., (2001). *Comparison of the three principal component analysis techniques to porphyry copper alteration mapping: a case study in Meiduk area, Kerman, Iran*. Canadian Journal of Remote Sensing, 27, 176-182.

Declaration

I, undersigned declare that this thesis is my original work and has not been presented for a degree in any other university, and that all sources of material used for the thesis have been duly acknowledged.

_____

Abera Fantaye Weldemariam

School of Graduate Studies

Jun, 2009

This Thesis has been submitted for examination with my approval as university adviser.

_____

Dagnachew Legesse (Ph.D.)